Mechanics of Materials 184 (2023) 104734

Contents lists available at ScienceDirect

Mechanics of Materials

journal homepage: www.elsevier.com/locate/mecmat

Research paper

Modeling of extremely ductile behavior of Zr-based bulk metallic glasses under compressive strain paths for solid-state processing

T. Barriere [a], X. Gabrion [b], S. Holopainen [c,*], N. Niang [a], J-M. Pelletier [d]

[a] Université de Franche-Comté, CNRS, Institut FEMTO-ST, F-25000 Besançon, France
[b] SUPMICROTECH, CNRS, Institut FEMTO-ST, F-25000 Besançon, France
[c] Tampere University, Department of Civil Engineering, FI-33014 Tampere, Finland
[d] Univ. de Lyon, CNRS, INSA-Lyon, MATEIS UMR5510, F-69621, France

ARTICLE INFO

Keywords:
BMGs
Plasticity
Softening & hardening
Modeling & Experimentation
Strain rate
Free volume & crystallization

ABSTRACT

In addition to extremely high strength, manufacturing temperatures of bulk metallic glasses (BMGs) relative to steels are low making them to desired energy saving engineering materials. However, BMGs are significantly brittle at low temperatures. To further increase suitability of BMGs for widespread use, it is essential to understand their plastic deformability (ductility) for high-tech solid-state processes at lowered temperatures. In this work, extremely large deformation behavior (near 80% in compression) of industrially important Zr-based BMGs was investigated. The experimentally measured results aided in the development of an appropriate constitutive model and revealed the micromechanisms affecting the characteristic macroscopic deformation behavior including softening and hardening. The measured and model results showed that the ductility can be significantly improved through chemical composition changes, such as a reduction in the Cu content and an increase in the Zr, Ti, or Be contents. In contrast to previously announced conclusions on the high glass-forming ability (GFA) being the precursors to ductility, formation of sufficiently low degree of crystallization during cooling improved ductility of as-cast specimens under loadings. These observed properties are important in assessing the ability of BMGs for solid-state processing.

1. Introduction

Bulk metallic glasses (BMGs) have been used since the 1960s. Here, "glass" refers to the solid state existing at temperatures below the glass transition temperature T_g (atoms are randomly arranged), and "bulk" refers to the volume of the material piece (Kruzic, 2016). The advantageous properties of BMGs are directly because of their non-crystalline structure existing without defects, such as dislocations, that occur in conventional crystalline metals and alloys (Zhang et al., 2020). Therefore BMGs can be formed into micro- and even nanostructures (mesoscopic structures).

BMG systems can be classified as ferromagnetic and non-ferromagnetic depending on their composition. The ferromagnetic systems include Fe-, Co-, and Ni-based systems, whereas the non-ferromagnetic group comprises of Ln-, Mg-, Zr-, Ti-, Pd-, Ca-, Cu-, Pt-, and Au-based systems (Zhou et al., 2021). This study focuses on industrially interesting ductile Zr-based BMGs, where Zr is the main component. In the 1990s, the discovery of Zr-based Vitreloy 1 BMG with a reasonable cooling rate was revolutionary because it enabled the development and production of orders of magnitude larger layers of amorphous structure (Kruzic, 2016; Ravichandran and Johnson, 2003; Telford, 2004). Using the existing manufacturing processes including optimized conditions nowadays, specimens made from BMGs are sufficiently large for vast amount of applications (casting thickness up to several centimeters), and they possess extremely high yield strength (~1.7 GPa), high elastic deformability (~5%), high thermal stability, and strong corrosion resistance (Zhou et al., 2021; Telford, 2004; Zhao et al., 2011; Fu et al., 2020).

The versatile processability of BMGs such as plastics (prior to the elastic limit), as well as their very high strength, makes BMGs suitable functional materials for high-tech electronic devices, nuclear reactors, aerospace, biomedicine, sporting goods, and surface coatings (cold spraying) (Zhang et al., 2020; Qiao and Pelletier, 2014; Han et al., 2021). Moreover, BMG pieces are widely employed as feedstock in other processes, such as thermoplastic forming (TPF) and laser welding (Zhu et al., 2014). The global metallic glass market size was USD 1.49 billion in 2019, and the highest increase in product consumption occurred in the electronics sector (Pulidindi and Mukherjee, 2020).

* Corresponding author.
E-mail address: sami.holopainen@tuni.fi (S. Holopainen).

https://doi.org/10.1016/j.mechmat.2023.104734
Received 23 February 2023; Received in revised form 12 June 2023; Accepted 25 June 2023
Available online 16 July 2023
0167-6636/© 2023 The Author(s). Published by Elsevier Ltd. This is an open access article under the CC BY license (http://creativecommons.org/licenses/by/4.0/).

However, a shortcoming of BMGs, especially at low temperatures, is their asymmetric deformation under tension and compression. BMGs are significantly brittle in tension and do not resist notable plastic deformations and long fatigue lives (Ravichandran and Johnson, 2003; Han et al., 2021; Fu et al., 2020; Zhu et al., 2021). Therefore, their applications are often limited to elastic tension and restrained compression conditions, showing an adequate uniformity to each other (Wu et al., 2008). The lack of ductility (high fracture toughness and plastic deformability) also in compression impedes the practical use of BMGs and their machinability (Qiao et al., 2016; Mu et al., 2021). To improve ductility, pure BMGs have conventionally been replaced by their granulate-based composites (BMGCs) consisting of a metallic glass matrix containing fibers or dendritic particles of ductile crystalline metals (Qiao and Pelletier, 2014; Fu et al., 2020; Cardinal et al., 2018; Lin et al., 2020; Gao et al., 2015; Krämer et al., 2017).

Most ductile (malleable) BMGs facilitate solid-state processing, such as mechanical alloying and cold working (forming, rolling, imprinting) at increased deformation rates and low temperatures (well below the glass transition temperature, T_g) and thus, reduce energy consumption (Kruzic, 2016; Han et al., 2021; Singh et al., 2016; Wang et al., 2017). Improving ductility at low temperatures can also increase ductility at high processing temperatures by reducing highly localized shear banding (Qiao et al., 2016). By improving ductility, the critical problem concerning the size limitation of BMG species can be solved, and larger components with complex shapes can be cast at lowered temperatures (Cardinal et al., 2018).

In practice, the ductility of BMGs can be improved through various methods such as ion irradiation, cryogenic thermal cycling, structural modification (e.g., cold rolling), and nanocrystallization (Han et al., 2021; Wu et al., 2008; Du et al., 2020; Yuan et al., 2022; Magagnosc et al., 2014; Luo et al., 2019). Moreover, ductility can be improved by surface treatments such as coatings (Kruzic, 2016). However, the increase in ductility reached by these methods have been limited to strains lower than 20%. Changing the chemical composition (micro-alloying) for improving ductility is more efficient method (Zhao et al., 2011; Fu et al., 2020; Qiao et al., 2016; Wu et al., 2010), and it is applied in this work.

Today, constitutive models that describe and predict mechanical behavior are important for the development and simulation of structural materials. Ductility is significantly influenced by the composition, which can change drastically within just one atomic percent. Consequently, a vast number of compositions are required to systematically scan the entire composition space, which is only possible with a capable simulation tool. The material characteristics of extremely ductile BMGs, including complex softening and hardening behavior (along with their modeling and simulation), have been almost ignored in the literature. In many studies, the deformation behavior of glassy metals is modeled by existing acceptable but coarse constitutive models that are actually not designed for glassy metals. For instance, Drucker–Prager-based models have been used to describe the plastic deformation behavior of granular materials, including BMGs, and their free-volume and pressure dependence (Han et al., 2021; Steif et al., 1982; Berdichevsky, 2014). However, these models, as such, have not been developed for very large plastic deformations (Berdichevsky, 2014). Chan et al. Zhao et al. (2021) applied an elastic-perfectly plastic constitutive model based on the Von Mises criterion to approximate the deformation behavior of Zr-based BMG. Guozheng et al. Wei et al. (2018) proposed a three-dimensional continuum model for BMGs based on the free volume theory. However, material behavior in these two studies showed solely small strains without softening.

When developing suitable models for glassy metals, including considerable deformations and softening, it is widely argued (through testing) the necessity of free-volume creation in shear bands (SBs) influencing strongly also macroscopic deformation behavior (asymmetric behavior, rate and temperature dependence) (Kruzic, 2016; Han et al., 2021; Luo et al., 2014; Zhao et al., 2019; Steif et al., 1982; Fan et al., 2016; Rao et al., 2019). Gong et al. Zhao et al. (2020) simulated the influence of the free-volume fraction and the shape and orientation of the free-volume region on the macroscopic deformation behavior of BMGs. They showed that the free volume is a precursor to plastic deformation, and the shape, orientation, and the yield strength of the free-volume regions have a limited effect on the macroscopic stress vs. strain response. However, the macroscopic strains only up to 20% were studied. In Lu et al. (2021), based on the MD simulations, sufficient loose atomic packing (probably the free volume) was reported to enhance the plastic deformability and ductility of Zr-based BMGs (compressive strains up to 25%). Shahabi et al. (2015) investigated the softening and fracture of a Zr-based BMG, both of which occurred before reaching a macroscopic compressive strain of 20%. In Anand and Su (2005) and Henann and Anand (2009), the effect of the free volume and notch root radius on the macroscopic deformation behavior and failure of different glassy metals were investigated. In addition, in these studies, the strains were limited to the maximum of 20%.

Due to the limitations of the previous models, a microstructure-based constitutive model is proposed, which is used to characterize the macroscopic low- to ultra-large deformation behavior of Zr-based BMGs under compressive strain paths at room temperature (RT). This thermodynamically relevant model includes the effect of hydrostatic stress and plastic dilatation, producing a strength asymmetry between tension and compression. Because chemical composition, a sufficient degree of crystallization, loading history, and loading rate are the most important factors influencing the ductility and plasticity of BMGs (close to RT) (Zhao et al., 2011), their effect to explain atomic-to-microstructural changes and the macroscopic deformation behavior (softening and hardening) is comprehensively discussed based on the data and model predictions.

2. Materials and methods

2.1. Manufacturing of specimens

The highly ductile Zr-based compositions $Zr_{65}Cu_{15}Ni_{10}Al_{10}$, $Zr_{52.5}Cu_{17.8}Ni_{14.5}Al_{10}Ti_5$, and $Zr_{40}Ti_{25}Cu_8Be_{27}$ (the composition is based on the nominal atomic percentage, at%) were found and delivered by a supplier from Xi'an, China. The glass transition temperature T_g of similar compositions are 630 K (Afonina et al., 2020), 670 K (Tournier, 2016), and about 600 K (Zong et al., 2016), respectively, reflecting the lower the T_g, the more ductile is the composition (Zhao et al., 2011).

These in situ BMGs were produced by suction (vacuum) casting. In this method, the BMG rods are directly manufactured from melted mother alloy (homogeneous alloy ingot not in amorphous state), followed by fast cooling. The metallic glasses were fabricated in two successive steps: (i) First, the formation of a mother alloy to obtain a material with the desired composition. For this purpose, the constituent elements of very high purity (99,99%) were mixed in the necessary quantities and then melted by arc melting under the argon atmosphered vacuum. Four successive melts were performed to ensure very high homogeneity. (ii) These master alloys were then remelted under vacuum and finally poured by suction casting into water-cooled copper molds.

It has been reported that a sufficiently large content of small enough crystalline particles in a tough bulk metallic matrix (BMGCs) is the most efficient way to increase ductility (Qiao and Pelletier, 2014; Fu et al., 2020; Cardinal et al., 2018; Krämer et al., 2017). It is also known that the phase separation (regions with different chemical ordering and degree of crystallization) may be developed in BMGs during casting (cooling of the mold) increasing ductility (Wang et al., 2018). In this basis, high ductility of the BMGs was achieved by allowing a sufficiently low degree of crystallization to be formed during the low enough cooling rate of the mold (Zhu et al., 2021; Hofmann, 2013), e.g., 160 K/s for $Zr_{65}Cu_{15}Ni_{10}Al_{10}$; when a metal liquid is cooled at a low rate, such as 1 K/s, the crystallization occurs. But when cooling down at a high enough cooling rate, such as 10...1000 K/s depending on the

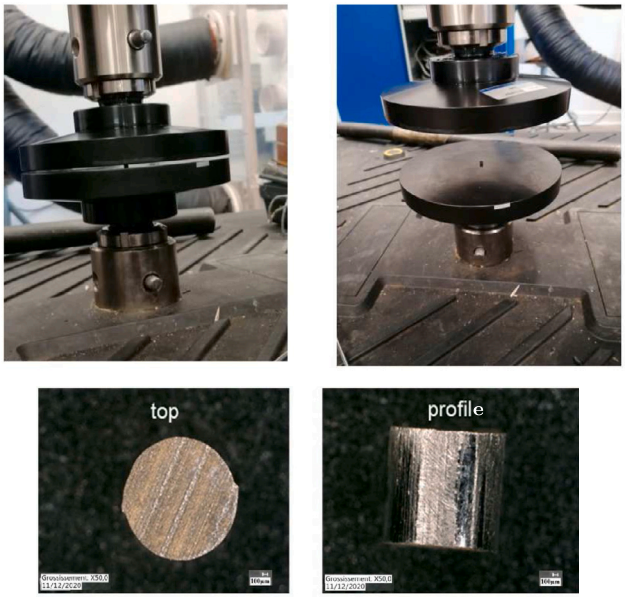

Fig. 1. Testing machine used (top). The test specimen stands out between the lower and upper platens, in the middle of them. Initial shape of the test specimens (bottom).

composition, the crystallization is suppressed and perfect BMGs are produced (Singh et al., 2016; Yin, 2013). Therefore, the material is not completely monolithic and includes both amorphous and crystalline (to a lesser extent <10%) phases.

The rods manufactured were cylindrical, with the diameter of 3 mm and the length of approximately 50 mm. The rods were subjected to the differential scanning calorimetry (DSC) at a temperature change rate of 3 K/min (in the high purity dry nitrogen atmosphere) and scanning electron microscope (SEM) imaging to confirm the glassy nature of the material. In compliance with the standard ASTM E9-89a (2000) for testing high-strength materials, the rods were cut into 3-mm-long pieces to obtain a nominal aspect ratio AR=height:diameter=1:1. This low AR, in contrast to 2:1 (Kruzic, 2016; Wu et al., 2008; Fan et al., 2016), enabled the observation of high plastic strains without premature buckling and failure during the applied compressive tests. Cutting was performed using electrical discharge machining (EDM). The shape of the test specimens is illustrated in Fig. 1. The glassy nature of specimens was further characterized by X-ray diffraction (XRD) experiments by using the Bruker D8 Discover diffractometer equipped with an Atlas goniometer.

The specimens were polished to minimize the surface roughness (by 20 μm SiC grinding papers). To further reduce geometrical imperfections, such as the tilt angle between the top/bottom of the specimen and platen of the testing machine, the cutting angle of the cutter was carefully verified, and the orthogonal shapes of the specimens were evident in the high-quality optical images taken before the tests.

2.2. Compression tests

Notably, there is no standard for testing large deformations in BMGs. The uniaxial tests at RT were performed on MTS criterion 45 machine equipped with a 100 kN load cell:

- monotonic, quasi-static displacement-controlled tests at the deformation rates of $V = 0.01$, 0.1, and 1 mm/s until rupture;
- progressively repeated load (PRL) tests that were displacement-controlled at the velocities of $V = 0.01$ and 0.1 mm/s. The unloadings were started when the stresses of 850 (elastic), 1450 (near to the yield stress), 1700, 2100, and 2800 MPa were reached (in the most brittle case, the last unloading was not achieved). The unloadings were performed until zero stress was reached.

The machine platens were placed next to each other and carefully adjusted before the tests, which were controlled in terms of the axial force F and speed of movement of the top platen, as demonstrated in Fig. 1. The corresponding axial strain rate is $\dot{\epsilon} = V/H$, where $H = 3$ mm is the initial height of the specimen. The engineering strain becomes $\epsilon = \Delta H/H$, where $\Delta H = h - H$ and h is the final height. The stress was calculated by $\sigma = F/A$, where A is the initial cross-sectional area of the specimen. This 1st Piola–Kirchhoff stress and the engineering strain were easy to measure and they were also applied in the model results.

The first test set was designed to observe the yield strength σ_y (the largest stress observed at the end of the elastic response), the corresponding yield strain, the Young's modulus (the value of the initial slope of the stress vs. strain curve), softening (stress drop), and hardening at very large strains. The second test set was designed to study material softening and hardening after the unloadings, followed by reloadings. The deformed shapes of the specimens after the tests were analyzed by the non-contact metrology by the Werth video-check machine.

3. Theory

Deformation and stress

To model large plastic deformations, a conventional approach (Kröner-Lee decomposition) where the total deformation gradient has the form

$$\boldsymbol{F} = \boldsymbol{F}^{\mathrm{e}}\boldsymbol{F}^{\mathrm{p}}, \quad J = \det(\boldsymbol{F}) > 0 \tag{1}$$

is applied. The decompositions $\boldsymbol{F}^{\mathrm{e}}$ and $\boldsymbol{F}^{\mathrm{p}}$ define the elastic and plastic contribution, respectively (Anand and Su, 2005). The polar decomposition

$$\boldsymbol{F}^{\mathrm{e}} = \boldsymbol{v}^{\mathrm{e}}\boldsymbol{R}^{\mathrm{e}} \tag{2}$$

defines the alignment of the elastic relaxed placement by the symmetric elastic stretch $\boldsymbol{v}^{\mathrm{e}}$ and the rotation $\boldsymbol{R}^{\mathrm{e}}$. Polar decomposition of $\boldsymbol{F}^{\mathrm{p}}$ is not applied because the plastic deformation is path-dependent when the relationship between plastic rotations and stretches is laborious to define (Barriere et al., 2020).

The stress, based on the Saint-Venant elastic potential, is given by (Holopainen and Barriere, 2018; Barriere et al., 2020):

$$\boldsymbol{\tau} = \tilde{E}/(1+\nu)\ln\boldsymbol{v}^{\mathrm{e}} + \tilde{E}/[3(1-2\nu)]\mathrm{tr}\,(\ln\boldsymbol{v}^{\mathrm{e}})\boldsymbol{i}, \tag{3}$$

where $\tilde{E} = (1-D)E$ (the Young's modulus E under high deformation rates is reduced by the damage, D), ν is the Poisson's ratio, and $\boldsymbol{i}$ is the identity tensor (results will be presented in terms of the 1st Piola–Kirchhoff stress $\boldsymbol{\sigma}$ with components (i, I) given as $\Sigma_{j=1}^{3}\boldsymbol{\tau}(i,j)\boldsymbol{F}^{-1}(I,j)$). The stress has the spectral decomposition

$$\boldsymbol{\tau} = \Sigma_{i=1}^{3}\tau_i\boldsymbol{e}_i \otimes \boldsymbol{e}_i, \ \tau_1 \geq \tau_2 \geq \tau_3, \tag{4}$$

where $\{\tau_i \mid i = 1,2,3\}$ denote the principal stresses, and $\{\boldsymbol{e}_i \mid i = 1,2,3\}$ correspond the orthonormal principal directions (Anand and Su, 2005; Henann and Anand, 2009).

The evolution of the plastic deformation in the position $\boldsymbol{X}$ is defined by

$$\dot{\boldsymbol{F}}^{\mathrm{p}} = \boldsymbol{L}^{\mathrm{p}}\boldsymbol{F}^{\mathrm{p}}, \ \boldsymbol{F}^{\mathrm{p}}(\boldsymbol{X}, t=0) = \boldsymbol{1}, \tag{5}$$

where the plastic flow given by the plastic velocity gradient $\boldsymbol{L}^{\mathrm{p}}$ is presumed to arise by shearing accompanied by dilatation (Luo et al., 2014) relative to certain slip systems as

$$\boldsymbol{L}^{\mathrm{p}} = \Sigma_{k=1}^{6}\dot{\gamma}_k^{\mathrm{p}}\boldsymbol{s}^{(\mathrm{k})} \otimes \boldsymbol{m}^{(\mathrm{k})} + \varsigma\dot{\gamma}_k^{\mathrm{p}}\boldsymbol{m}^{(\mathrm{k})} \otimes \boldsymbol{m}^{(\mathrm{k})}. \tag{6}$$

Each slip system is specified by the slip direction $\boldsymbol{s}^{(\mathrm{k})}$, slip normal $\boldsymbol{m}^{(\mathrm{k})}$, shearing rates $\dot{\gamma}_k^{\mathrm{p}}$, and average (microscopic) dilatation function ς (Anand and Su, 2005) defined below.

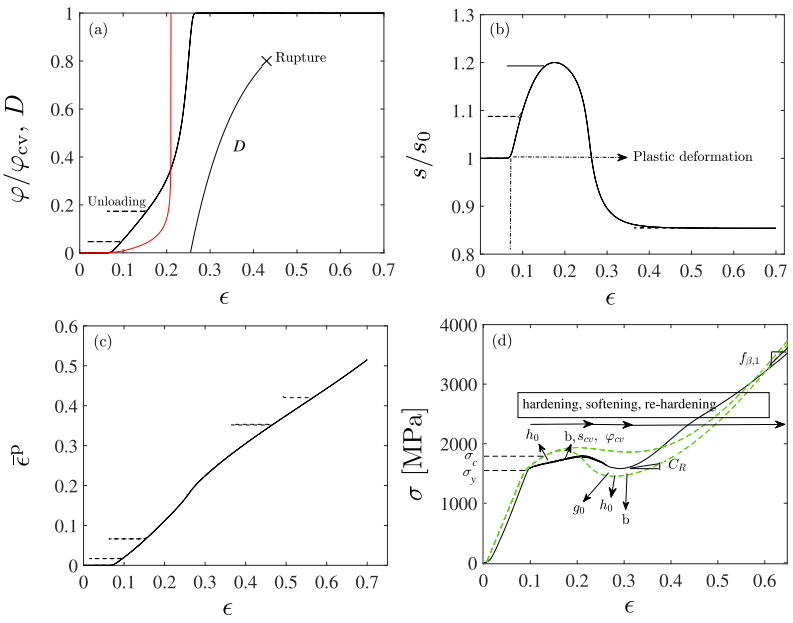

Fig. 2. Development of the internal variables φ (a) and s (b) (based on the fitted parameters) when $\dot{\epsilon} = 0.003$ /s during PRL (dashed curve) and monotonic loading (solid curve). Development of the free volume by the Spaepen's model (Han et al., 2021) (red curve, monotonic loading) and damage (D, black solid curve, monotonic loading) are also shown (a). The corresponding development of the accumulated plastic strain $\bar{\epsilon}^p$ (c). The effects of the material parameters on the shape of hardening, softening, and re-hardening (green dashed lines) (d). The arrows indicate an increase in a parameter, and the data are shown in black. (For interpretation of the references to color in this figure legend, the reader is referred to the web version of this article.)

Yielding and softening - effect of the free volume

The observed, specific hardening–softening behavior of the most ductile BMGs is characterized by a reduced stress development that occurs in two successive stages during increased deformations: first, a reduced stress development followed by the second, intense stress drop, Fig. 2(d). The first stage is characterized by the relation $\sigma_y < \sigma_c$, where σ_y and σ_c are the yield strength and the second (upper) yield strength, respectively (the strain ϵ_c of σ_c, before the stress drop, is greater than of σ_y, see Fig. 2(d)). If this condition is violated (i.e., $\sigma_y > \sigma_c$), the behavior is much more brittle: just a softening followed by a rapid failure (Wu et al., 2008; Zhou et al., 2018), or the high ductility can be achieved by reducing significantly the strain rate (Qiu et al., 2012). Similar hardening–softening behavior for $Zr_{55.7}Cu_{22.4}Ni_{7.2}Al_{14.7}$ has been evidenced in Zhu et al. (2021), but with limited strains (15%) and rates (5E-5 /s).

The hardening–softening behavior described above is presumed to be directly related to the two-phase disordering of the material (slow disordering followed by a rapid one affecting dilatation) where the second phase (softening) is due to the propagation of the primary SBs under rapid localization of plastic flow (Qiu et al., 2012; Pan et al., 2020; Songa et al., 2021). The disordering in the first phase (hardening) is described by either a shear transformation zone (STZ by Argon, 1979) or a local atomic jump (by Spaepen, 1977) (Schuh et al., 2007). STZ is a local cluster of atoms that undergoes rearrangement to form a higher free-volume and energy configuration. A multitude of STZs generates SBs, and the greater the number and density of SBs, the greater the plastic deformation (Zhu et al., 2021). The disordering is further associated with the creation of additional free volume within SBs (Zhang et al., 2020; Ravichandran and Johnson, 2003; Han et al., 2021; Luo et al., 2014; Jiang et al., 2015). The free volume represents the disordering zones where atomic or nanoscopic structures can move without resulting in an energy change (Zhao et al., 2020). In other words, the free volume describes the extra volume for disordering zones relative to an ideal and fully dense amorphous state, as can be reached for a super-cooled liquid, i.e., free volume can be determined e.g., by DSC (Kruzic, 2016). Then, the initial propagation of SBs in BMGs can be quantitatively described by the localized free-volume evolution (Luo et al., 2014; Zhao et al., 2020).

Table 1
Spaepen model parameters for $Zr_{65}Cu_{15}Ni_{10}Al_{10}$. The values $f\exp(-\Delta G^m/k_BT) = 1E7$ (Han et al., 2021) and $k_{fv} = 25.585635$ (requires very high accuracy) has been used.

Parameter	E	ν	a	τ_0	β	k_{DP}	n_D
Unit	GPa			GPa			
Value	20	0.37	0.2	0.4	0.9	0.4	4

The development of the free volume from its initial concentration φ_0 to $1.5\varphi_0$ according to the Spaepen's model (Han et al., 2021) is

$$\dot{\varphi} = \frac{f}{a} e^{-\frac{\Delta G^m}{k_B T}} e^{-\frac{1}{k_{fv}\varphi}} \left[\frac{3(1-\nu)}{E}\frac{\tau_0}{\beta\varphi}\left\{\cosh\left(\frac{\tau_{DP}}{\tau_0}\right) - 1\right\} - \frac{1}{n_D}\right], \tag{7}$$

where $\tau_{DP} = \sqrt{\mathrm{tr}(3/2(\boldsymbol{\tau}^{dev})^2)} + k_{DP}\mathrm{tr}(1/3\boldsymbol{\tau})$ and $\boldsymbol{\tau}^{dev} = \boldsymbol{\tau} - \mathrm{tr}(1/3\boldsymbol{\tau})$. Because the plastic evolution in the Spaepen's model (Steif et al., 1982) is not a function of the local state of the material at any given instant as it should be (Anand and Su, 2005), especially during the transients associated with disordering during softening, the plastic evolution is defined here by the law (5). Moreover, the Spaepen's model describes the disordering of the material based on a local atomic jump (atomic level) with high free-volume concentrations ~ 0.05, whereas the initial free-volume concentration in as-cast specimens, on average in the micro- to macro-level, is considered low, $\varphi_0 = 0.001$ (Anand and Su, 2005; Henann and Anand, 2009). When trying to apply (7) in higher dimensions, a large enough scaling parameter k_{fv} was used to compensate the low value φ ($k_{fv} = 1$ in the Spaepen's model Han et al., 2021). The corresponding model parameters for the uniaxial compressive stress are given in Table 1, and the free volume development is shown in Fig. 2(a).

However, calculations were observed to be sensitive to k_{fv} and therefore, an evolution law, suitable to evaluate the average free volume development in micro- to macro-level, is proposed. Plastic flow occurs by initial multiple SBs resulting in shear-dominated sliding accompanied by dilatation relative to a slip system, cf. Eq. (6). The dilatation rate on each plane of the slip system is averagely defined by the shear-induced plastic dilatancy function

$$\varsigma = g_0(1 - \varphi/\varphi_{cv}), \tag{8}$$

where φ_{cv} is a positive material parameter representing the maximum or the saturation value of the free volume (Anand and Su, 2005; Henann and Anand, 2009). The free volume representing the average volume (dilatation in microscale) for multiple disordering zones evaluates according to

$$\dot{\varphi} = \varsigma \dot{\gamma}^{\mathrm{p}}, \ \varphi(0) = \varphi_0, \tag{9}$$

where the plastic deformation rate $\dot{\gamma}^{\mathrm{p}} \geq 0$ is subsequently defined. The material dilates when $\varsigma > 0$ and $\varphi < \varphi_{cv}$.

Contrary to preceding works (Anand and Su, 2005; Henann and Anand, 2009) for brittle BMGs, where g_0 is considered to be a constant parameter, the most ductile BMGs show hardening-softening behavior which characteristic requires g_0 to be modified:

$$\hat{g}_0 = \min(g_0 e^{g_1(\bar{\epsilon}^{\mathrm{p}})^q}, {g_0}^{\mathrm{u}}) \tag{10}$$

with additional parameters g_1 and q, and a large enough upper limit, ${g_0}^{\mathrm{u}}$ =1E10. The cumulative plastic strain

$$\bar{\epsilon}^{\mathrm{p}} = \int \dot{\bar{\epsilon}}^{\mathrm{p}} \mathrm{d}t \ \text{ with } \ \dot{\bar{\epsilon}}^{\mathrm{p}} = \sqrt{2/3 \, \mathrm{tr}\left((\boldsymbol{D}^{\mathrm{p}})^2\right)} \tag{11}$$

shown in Fig. 2(c) is constantly increasing and takes the loading history into consideration; experiments show that the nucleation of nano-defects (SBs including free volume) initiates when a certain value of the cumulated plastic strain is reached (Lemaitre and Desmorat, 2001)(Section 6.14). The cumulated plastic strain enables, as shown below, the prediction of hardening-softening characteristic: g_0 reduces the stress, see Fig. 2(d), and the value of $\hat{g}_0$ in the hardening stage (transition from STZs to SBs) is small compared to that in the softening (governed by SBs) because of the exponent function of $\bar{\epsilon}^{\mathrm{p}}$, where $\bar{\epsilon}^{\mathrm{p}}$ is yet raised to the q power. The parameters needed in the proposed evolution model (8)–(10) are easy to determine from the macroscopic stress vs. strain curve. The evolution of the free volume is demonstrated in Fig. 2(a).

Yielding and softening - effect of the strain rate

The effect of the strain rate on the macroscopic deformation behavior under quasi-static loadings is typically small, especially when the composition is ductile (Zhou et al., 2018). However, a small reduction in the yield stress with increasing strain rates can be observed, see Fig. 3. This characteristic contrasts that of crystalline metals and glassy polymers, whose yield stress increases with strain rate (Zhu et al., 2021; Zhou et al., 2018; Barriere et al., 2020). In fact, the issue with the closest state-of-the-art models (Anand and Su, 2005; Henann and Anand, 2009) for BMGs is that the yield stress increases with increasing strain rate. Moreover, the previous models cannot reproduce a marked softening, let alone the hardening-softening behavior, which was observed to be an inherent characteristic of most ductile BMGs at ambient temperature, cf. also (Qiu et al., 2012; Zhu et al., 2021). Contrary to the conventional elastic–plastic theory for metals, a specific yield criterion is not defined, but the elastic limit and yielding followed by softening are all defined by the isotropic shear resistance s to the plastic flow in the isotropic material being the same for all planes of the slip system (scalar) (Anand and Su, 2005; Henann and Anand, 2009). The isotropy of the material was evidenced by the rapid rupture of the specimens, i.e., no notable inhomogeneity (cracking yielding anisotropy) was not observed before rupture. To capture the rate-dependent hardening–softening behavior, the evolution of s is modeled by

$$\dot{s} = s_{\mathrm{T}}(1 - s/S)(\dot{\gamma}^{\mathrm{p}})^{h_{\mathrm{B}}}, \ s_{\mathrm{T}} = \hat{h}_0[e^{-h_{\mathrm{T}}(\bar{\epsilon}^{\mathrm{p}})^q}], \ s(0) = \hat{s}_0, \tag{12}$$

where $S = \hat{s}_{cv}(1 + b(\varphi_{cv} - \varphi))$ has been previously used instead of s for brittle BMGs (without hardening nor softening) (Henann and Anand, 2009). The term $(1-s/S)(\dot{\gamma}^{\mathrm{p}})^{h_{\mathrm{B}}}$ representing the rate of the plastic shear resistance was motivated by similar softening behavior of glassy polymers generated primarily due to shear banding (SB) (Anand and Ames, 2006; Barriere et al., 2020). The saturation value S decreases due to the increase of the free volume, and finally, $s = S = \hat{s}_{cv}$. The proposed evolution of s is shown in Fig. 2(b) and its comparison with Fig. 2(a, d) reveals that when the free volume reaches its maximum after the hardening (SBs subordinate STZs), s and subsequently the macroscopic stress show a rapid drop, i.e., softening due to the rapid propagation of SBs. The term s_{T} represents the reducing shear resistance during transition from STZs to SBs which causes stress relaxation and reduces the effect of the strain rate on the stress response during hardening.

The details for s_{T} and the effect of material parameters $\hat{h}_0$, h_{T}, h_{B}, $\hat{s}_0$, $\hat{s}_{cv}$, and b on the macroscopic deformation behavior are discussed subsequently in the calibration Section 3.2. The values of $\hat{s}_{cv}$, $\hat{s}_0$, and $\hat{h}_0$ were observed to strongly depend on the chemical composition, which the topic is discussed in Appendix A. With well-defined parameters the development of s (12) together with the free volume φ (8) allows the capture of the complex hardening–softening characteristic, as shown in Figs. 2(a–d): s reacts abruptly to φ and $\bar{\epsilon}^{\mathrm{p}}$ when deformation and its rate increase, thanks to the power functions of $\dot{\gamma}^{\mathrm{p}}$ and $\bar{\epsilon}^{\mathrm{p}}$ applied in the evolution Eqs. (8) and (12).

Evolution of the plastic deformation

During hardening, SBs diffuse and no preferred directions of slip planes for the system can be observed similar to those of crystalline and dislocated metals (Zhou et al., 2018). Therefore, the slip system is considered with respect to the principal directions of stress (Eq. (4)) (Anand and Su, 2005; Henann and Anand, 2009; Zhou et al., 2018):

$$\begin{aligned}
&\boldsymbol{s}^{(1)} = \cos\xi \boldsymbol{e}_1 + \sin\xi \boldsymbol{e}_3, \ \boldsymbol{m}^{(1)} = \sin\xi \boldsymbol{e}_1 - \cos\xi \boldsymbol{e}_3,\\
&\boldsymbol{s}^{(2)} = \cos\xi \boldsymbol{e}_1 - \sin\xi \boldsymbol{e}_3, \ \boldsymbol{m}^{(2)} = \sin\xi \boldsymbol{e}_1 + \cos\xi \boldsymbol{e}_3,\\
&\boldsymbol{s}^{(3)} = \cos\xi \boldsymbol{e}_1 + \sin\xi \boldsymbol{e}_2, \ \boldsymbol{m}^{(3)} = \sin\xi \boldsymbol{e}_1 - \cos\xi \boldsymbol{e}_2,\\
&\boldsymbol{s}^{(4)} = \cos\xi \boldsymbol{e}_1 - \sin\xi \boldsymbol{e}_2, \ \boldsymbol{m}^{(4)} = \sin\xi \boldsymbol{e}_1 + \cos\xi \boldsymbol{e}_2,\\
&\boldsymbol{s}^{(5)} = \cos\xi \boldsymbol{e}_2 + \sin\xi \boldsymbol{e}_3, \ \boldsymbol{m}^{(5)} = \sin\xi \boldsymbol{e}_2 - \cos\xi \boldsymbol{e}_3,\\
&\boldsymbol{s}^{(6)} = \cos\xi \boldsymbol{e}_2 - \sin\xi \boldsymbol{e}_3, \ \boldsymbol{m}^{(6)} = \sin\xi \boldsymbol{e}_2 + \cos\xi \boldsymbol{e}_3,
\end{aligned} \tag{13}$$

where $\xi = \pi/4 + \phi/2$, $\phi = \arctan(\mu_c)$, and $\mu_c > 0$ is an internal friction coefficient (COF). Fig. 3 shows the distribution of the inverse quality factor Q_{loc}^{-1} of a Pd-based BMG, where Q_{loc}^{-1} corresponding to the maximal frequency represents the internal COF (Wagner et al., 2014). The idea of the slip system is demonstrated in Fig. 4: in the material point $\boldsymbol{x}_1$, the two slip systems $(\boldsymbol{s}^{(1)}, \boldsymbol{m}^{(1)})$ and $(\boldsymbol{s}^{(2)}, \boldsymbol{m}^{(2)})$ lies in certain $(\hat{\boldsymbol{e}}_1, \hat{\boldsymbol{e}}_3)$-plane (e.g., containing the maximum and minimum principal stress directions). The orientation of the slip system in a second material point of the plane is different because the local stress states at these two points are in general different. The plastic deformation at a nanoscopic level occurs by local shear transformations of material clusters in SBs and it occurs in the slip directions. This shearing is accompanied by deformation-induced microstructural disordering and plastic dilatation (Henann and Anand, 2009). At the macroscopic level, the collective action of numerous such shear transformations is represented by local averaged plastic shearing rates $\dot{\gamma}_k^{\mathrm{p}}$, and the resulting plastic velocity gradient $\boldsymbol{L}^{\mathrm{p}}$ (6).

The normal traction σ_{k} (greater than zero in compression) and the shear traction τ_{k} (lower than zero in compression) on each slip plane of the system are defined by

$$\sigma_{\mathrm{k}} = -\boldsymbol{m}^{(\mathrm{k})} \cdot \boldsymbol{\tau} \boldsymbol{m}^{(\mathrm{k})}, \ \tau_{\mathrm{k}} = \boldsymbol{s}^{(\mathrm{k})} \cdot \boldsymbol{\tau} \boldsymbol{m}^{(\mathrm{k})}, \tag{14}$$

and the evolution of shearing deformation (almost plastic) in each plane is

$$\dot{\gamma}^{\mathrm{p}}{}_{\mathrm{k}} = \dot{\gamma}_0(\bar{\tau}/(s - k_1\tau_{\mathrm{k}} - k_2\mu_c\sigma_{\mathrm{k}}))^{(1/m)} \geq 0 \tag{15}$$

when $\bar{s} = s - k_1\tau_{\mathrm{k}} - k_2\mu_c\sigma_{\mathrm{k}} > 0$ and $\dot{\gamma}^{\mathrm{p}}{}_{\mathrm{k}} = 0$ otherwise. The parameters are $\dot{\gamma}_0$, k_1, k_2, and m, and s is the shear resistance representing the softening behavior defined above. Noting that $\bar{\tau}/\bar{s} = (\dot{\gamma}^{\mathrm{p}}{}_{\mathrm{k}}/\dot{\gamma}_0)^m$, the limit $m \to 0$ renders the theory rate-independent. It also turns out that $\bar{\tau}/\bar{s}$ in (15) acts as a driving force for all the slip systems. Contrary

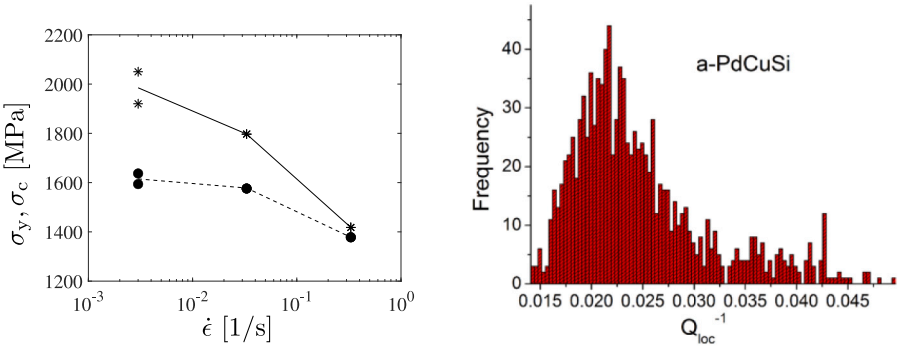

Fig. 3. Yield strengths σ_y (dashed) and σ_c (solid) vs. strain rate of $Zr_{65}Cu_{15}Ni_{10}Al_{10}$ (left). The frequency of the inverse quality factor Q_{loc}^{-1} of a Pd-based BMG corresponding to the maximal frequency and representing the internal COF (Wagner et al., 2014) (right).

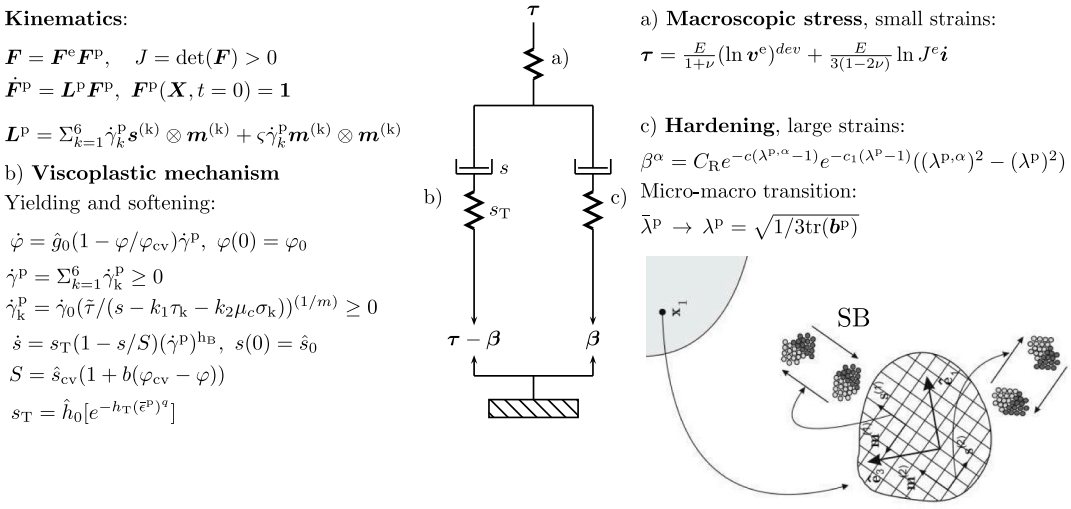

Fig. 4. Rheological representation of the model: a) an elastic spring, b) a nonlinear system consisting of a viscoplastic dashpot (combination of two dashpots for STZs (s_{T}) and SBs (s)) and a viscous spring (for s_{T}), and c) a nonlinear system consisting of a viscous dashpot and a nonlinear spring. Evolution equations for the internal variables φ (free volume) and s (shear resistance) are presented. Schematics of plastic flow by SBs on microscopic slip systems (bottom right).

to the previous state-of-the-art models (Anand and Su, 2005; Henann and Anand, 2009), τ_k in the numerator is replaced by the reduced equivalent stress $\tilde{\tau} = \sqrt{\mathrm{tr}\,(\tilde{\boldsymbol{\tau}}^2)/2}$, with $\tilde{\boldsymbol{\tau}} = \boldsymbol{\tau} - \boldsymbol{\beta}$ incorporating the hydrostatic stress $1/(3J)\mathrm{tr}\,(\boldsymbol{\tau})$ and the backstress $\boldsymbol{\beta}$ (defined below) for hardening at extreme large strains. Therefore, $\dot{\gamma}^{\mathrm{p}}{}_{\mathrm{k}}$ results in dilatational plasticity (volume change $J^{\mathrm{p}} = \det(\boldsymbol{F}^{\mathrm{p}}) > 0$). It has been shown that hydrostatic stress affects the formation of localized free volume and SB, explaining the asymmetry between tension and compression (Zhao et al., 2019; Rao et al., 2019): compressive hydrostatic stress can suppress the generation of free volume and restrict SB. The shear traction τ_k in the denominator tends to reduce $\dot{\gamma}^{\mathrm{p}}{}_{\mathrm{k}}$ in compression, as in the previous models (Anand and Su, 2005; Henann and Anand, 2009). Contrary to the previous models, especially the model (Henann and Anand, 2009) for ambient temperature, the friction μ_c tends to slightly increase $\dot{\gamma}^{\mathrm{p}}{}_{\mathrm{k}}$ to averagely model an expected reduction of friction during hardening (due to fracturing and temperature rise). The effect of friction is constrained by a small enough parameter, k_2. The sum of the shearing rates on all planes of the slip system

$$\dot{\gamma}^{\mathrm{p}} = \Sigma_{k=1}^{6}\dot{\gamma}^{\mathrm{p}}{}_{\mathrm{k}} \tag{16}$$

gives the total plastic shearing rate at a material point and represents the local development of the plastic deformation.

Hardening - extreme strains

The stress vs. strain responses of the most ductile BMGs showed hardening also at extremely large strains (increase in stress with an increase in plastic strain greater than 0.25). In the proposed continuum model, the backstress $\boldsymbol{\beta}$ accounts for this re-hardening. Considering the deformation of initially cubic microscopic material element, the microscopic plastic stretching in the diagonal direction $\bar{\boldsymbol{m}} = \sum_\alpha \bar{m}_\alpha \bar{\boldsymbol{N}}_\alpha$ with the components $\bar{m}_1 = \sin\bar{\theta}\cos\bar{\varphi}$, $\bar{m}_2 = \sin\bar{\theta}\sin\bar{\varphi}$, and $\bar{m}_3 = \cos\bar{\theta}$ is given by $\bar{\lambda}^{\mathrm{p}} = r/r_0$, where r and r_0 are the current and initial diagonal dimensions, respectively, see Fig. 5. The microscopic material clusters along the diagonal interact, deform, and align with the macroscopic deformation described by the unit vector $\bar{\boldsymbol{N}} := 1/\sqrt{3}\sum_\alpha \bar{\boldsymbol{N}}_\alpha$, and the macroscopic effective plastic stretch

$$\lambda^{\mathrm{p}} = \sqrt{\bar{\boldsymbol{N}} \cdot \boldsymbol{b}^{\mathrm{p}}\bar{\boldsymbol{N}}} = \sqrt{1/3\mathrm{tr}(\boldsymbol{b}^{\mathrm{p}})} = \sqrt{1/3\sum(\lambda^{\mathrm{p},\alpha})^2}, \tag{17}$$

where the unit eigenvectors $\bar{\boldsymbol{N}}_\alpha$, $\alpha = 1,2,3$, are the principal directions of $\boldsymbol{b}^{\mathrm{p}} = \boldsymbol{F}^{\mathrm{p}}\boldsymbol{F}^{\mathrm{p},T}$ and $\lambda^{\mathrm{p},\alpha}$ are the principal plastic stretches.

The stored energy φ^{p} of the backstress for hardening consists of the stored energies of the elements, and the backstress, applying the chain rule, is

$$\boldsymbol{\beta} = 2sym\Big(\frac{\partial\varphi^{\mathrm{p}}(\lambda^{\mathrm{p}})}{\partial\lambda^{\mathrm{p}}}\frac{\partial\lambda^{\mathrm{p}}}{\partial\boldsymbol{b}^{\mathrm{p}}}\boldsymbol{b}^{\mathrm{p}}\Big), \tag{18}$$

see Holopainen and Barriere (2018). Differentiation of (17) and multiplication by $\boldsymbol{b}^{\mathrm{p}}$ yield

$$2\frac{\partial\lambda^{\mathrm{p}}}{\partial\boldsymbol{b}^{\mathrm{p}}}\boldsymbol{b}^{\mathrm{p}} = \frac{1}{3\lambda^{\mathrm{p}}}\boldsymbol{b}^{\mathrm{p}}. \tag{19}$$

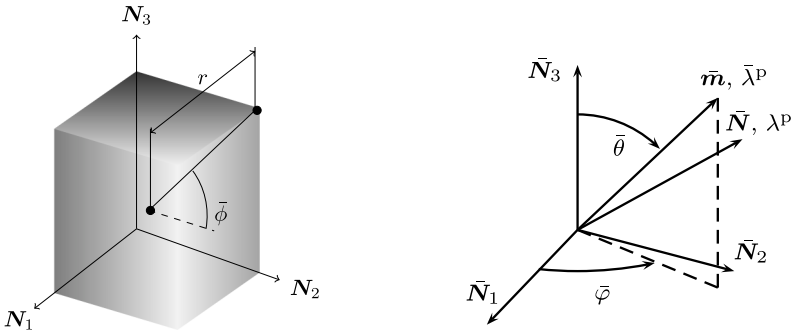

Fig. 5. Deformed microscopic material element (right). The unit base vectors $\bar{N}_\alpha$ of N_α, $\alpha = 1,2,3$, align with the eigenvectors of b^p. The diagonal is given by $r = \sqrt{3}/2a_0\bar{\lambda}^p$, where a_0 is the dimension of the undeformed element and $\bar{\lambda}^p = r/r_0$ denotes the plastic stretch which appears in the diagonal direction $\bar{m}$. The unit vector $\bar{m}$ is defined by the angles $\bar{\theta}$ and $\bar{\varphi}$, whereas the effective plastic stretch λ^p is related to the direction $\bar{N}$.

Substitution of (19) into (18) yields

$$\boldsymbol{\beta} = f_\beta \boldsymbol{b}^p,\ f_\beta = \frac{1}{3\lambda^p}\frac{\partial \varphi^p}{\partial \lambda^p} \geq 0. \tag{20}$$

Defining $f_\beta := C_R f_{\beta,1}(\lambda^p) f_{\beta,2}(\lambda^{p,\alpha})$, where C_R is the initial hardening modulus. In Wang et al. (2018) was concluded that the phase separation during casting results in some crystallization which also was the underlying mechanism for hardening of the Zr-based BMG applied. Therefore, in general C_R is an increasing function of the degree of crystallization, although it is considered a constant here because only a single evidence of the degree of crystallization (DC) was observed (discussed in the subsequent Section 4.2). The larger C_R and β^α (and DC), the greater the hardening is, as can be concluded from (15) for $\dot{\gamma}^p{}_k$ (including the reduction of $\tilde{\tau}$). If no crystallization occurs, C_R and the backstress $\boldsymbol{\beta}$ are considered zero, and no hardening evolves. Then, the first term defined by $f_{\beta,1} = \exp(-c_1(\lambda^p - 1))$, c_1 is material parameter determined in the calibration Section 3.2, describes the ultimate limit of the backstress due to notable SB affecting increase in the plastic strain and finally failure as the main SBs recur and intersect (Telford, 2004; Zhao et al., 2020; Shahabi et al., 2015). The reducing effect of the $f_{\beta,1}$ ($\lambda^p \geq 1$) on hardening is shown in Fig. 6. The second term, $f_{\beta,2} = \exp(-c(\lambda^{p,\alpha} - 1))$ (c is material parameter) being increasing in compression ($\lambda^{p,\alpha} \leq 1$), represents diffusionless disordering of the material after softening (Wu et al., 2010), which is associated with extremely localized plastic flow in SBs (Telford, 2004; Zhao et al., 2020; Shahabi et al., 2015); yet more dissipation energy is required for SB and deformation resulting in hardening.

Based on the proposed functions $f_{\beta,1}$ and $f_{\beta,2}$ the stored energy φ^p is subsequently obtained in Section 3.1. Considering the backstress deviatoric, the principal components are defined, in accordance with (20), as

$$\beta^\alpha = C_R f_{\beta,1}(\lambda^p) f_{\beta,2}(\lambda^{p,\alpha})((\lambda^{p,\alpha})^2 - (\lambda^p)^2),\ \alpha = 1,2,3. \tag{21}$$

The multiplicative composition of the terms $f_{\beta,1}$ and $f_{\beta,2}$ in (21) results in the desired development of the backstress and hardening. In tension, when $\lambda^{p,\alpha} \geq 1$ and $\lambda^p \geq 1$, the backstress remains negligible, and hardening does not occur, see Fig. 6(right). This characteristic is in accordance with the measurements which do not show hardening under tension at RT (Zhao et al., 2011).

3.1. Thermodynamic relevancy

Thermodynamic treatments of the constitutive models for amorphous materials based on the principle of virtual power have been reported in Holopainen and Barriere (2018) (viscoelastic–viscoplastic including damage, D) and Anand and Su (2005) (elastic–viscoplastic). According to these treatments, the localized plastic dissipation for the proposed elastic–viscoplastic model including damage becomes

$$\mathcal{D} = \tilde{\boldsymbol{\tau}} : \boldsymbol{L}^p - \dot{D}\frac{\partial \varphi^D}{\partial D} \geq 0. \tag{22}$$

It is required that $\dot{D} \geq 0$ (damage never decreases) and the damage potential φ^D, what ever it is, is reducing with respect to the damage. The proposed damage development determined in Appendix C and showed in Fig. 2(a) is a suitable one. Then, using (6) and (14) in (22), one obtains

$$\mathcal{D} = \Sigma_{k=1}^{6}\dot{\gamma}^p{}_k(\tilde{\tau}_k - \varsigma\tilde{\sigma}_k) + \dot{D}Y \geq 0, \tag{23}$$

where $\tilde{\sigma}_k = -\boldsymbol{m}^{(k)} \cdot \tilde{\boldsymbol{\tau}}\boldsymbol{m}^{(k)}$ and $\tau_k = \boldsymbol{s}^{(k)} \cdot \tilde{\boldsymbol{\tau}}\boldsymbol{m}^{(k)}$ and $Y = -\partial\varphi^D/\partial D \geq 0$. Omitting damage ($\dot{D}Y \geq 0$), $\tilde{\tau}_k - \varsigma\tilde{\sigma}_k \geq 0$, which is a restriction that the dilatancy function, ς, must satisfy for each k. During softening, $\boldsymbol{\beta}$ is not generated when $\tau_k - \varsigma\sigma_k \geq 0$ holds true. Using this restriction in the denominator of (15) for $\dot{\gamma}^p{}_k$ yields

$$\varsigma s - (\varsigma k_1 + \mu_c k_2)\tau_k > 0. \tag{24}$$

Otherwise, $\dot{\gamma}^p{}_k = 0$ in (15). Before hardening at extremely large strains, ς reaches its minimum zero, when (24) reduces to $-\mu_c k_2 \tau_k > 0$, i.e., plastic deformation in each system evolves only if $\tau_k < 0$. This constraint also holds true during hardening because the reduced stress measures $\tilde{\sigma}_k$ and $\tilde{\tau}_k$ are not included in the denominator of (15) for $\dot{\gamma}^p{}_k$. Moreover, this constraint restricts plastic deformation practically in tension, cf. (14), which is a typical characteristic of glassy metals.

Stored energy φ^p for hardening at extreme strains

It follows from (20)(right), after the integrations in parts, that

$$\varphi^p = \frac{3C_R}{cc_1}\left(\sum_{\alpha=1}^{3}\left(\frac{1}{\lambda^{p,\alpha}}\exp(-c_1(\lambda^p - 1))\exp(-c(\lambda^{p,\alpha} - 1))\right) - 3\right) \geq 0, \tag{25}$$

$\varphi^p(\lambda^p(\lambda^{p,\alpha})) = 0$ when $\lambda^p = \lambda^{p,\alpha} = 1$, in which treatment $\exp(-c(\lambda^p - 1))/\lambda^{p,\alpha}$ is virtually unity during hardening (in compression; the hardening does not occur in tension) was used, $c < c_1$, and the terms multiplied by $1/(c_1)^2$ relative to $1/c_1$ was omitted (c_1 is a magnitude greater than unity, see the calibration Section 3.2). Based on the calibrated parameters c and c_1 the error between the f_β proposed and that obtained from (20)(right) by using (25) was found (numerically) to be less than 10%.

3.2. Calibration of the model

The model was calibrated using uniaxial monotonic compression data for the reference material $Zr_{65}Cu_{15}Ni_{10}Al_{10}$ at RT and at $\dot{\epsilon} = 0.003$ /s, see Table 2 and Fig. 9(a). Prior to yielding, the material deforms elastically, that is, it returns to its original shape when the applied stress is withdrawn. The Young's modulus E corresponds to this slope of the initial response. The Poisson's ratio ν was determined from the Werth video-check results. The glass transition temperature of the applied Zr-based BMGs was 645 K, and under room temperature conditions, the quasi-static mechanical response was observed to be rather rate insensitive (Zhou et al., 2018). Therefore, low values of the strain-rate

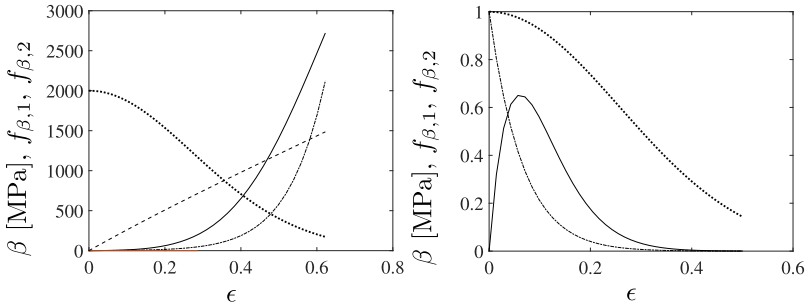

Fig. 6. Development of the axial backstress component (solid) and its functions $2E3 \cdot f_{\beta,1}$ and $f_{\beta,2}$ (dotted and dash-dotted) under compression (negative ϵ) (left). The difference $2E3 \cdot ((\lambda^{\mathrm{p},1})^2 - (\lambda^{\mathrm{p}})^2)$ (dashed) is also shown. The axial backstress component, $f_{\beta,1}$, and $f_{\beta,2}$ under tension (right).

Table 2
Comparison of the yield strengths σ_y and σ_c, and the corresponding yield strains ϵ_y and ϵ_c of Zr-based BMGs (mean values). The applied strain rates are also shown.

Monotonic tests					
Material's ID	σ_y (MPa)	σ_c (MPa)	ϵ_y (-)	ϵ_c (-)	$\dot{\epsilon}$ (s^{-1})
$Zr_{65}Cu_{15}Ni_{10}Al_{10}$ (i)	1,590	1,950	0.11	0.31	0.003
$Zr_{57}Cu_{20}Ni_8Al_{10}Ti_5$ (ii)	1,810	1,850	0.02	0.09	0.0001
$Zr_{48}Cu_{45}Al_7$ (iii)	1,820	1,720	0.02	0.04	0.0001
$Zr_{65}Cu_{18}Ni_7Al_{10}$ (iv)	1,390	1,340	0.02	0.12	0.005
$Zr_{52.5}Cu_{17.8}Ni_{14.5}Al_{10}Ti_5$ (v) ..	1,840	2160	0.12	0.24	0.003
$Zr_{40}Ti_{25}Cu_8Be_{27}$ (vi)	1,730	–	0.12	–	0.003

sensitivity parameters $\dot{\gamma}_0$ and m were used for all compositions (Anand and Su, 2005). The initial value for the coefficient of friction μ_c (COF) was taken from (Anand and Su, 2005). The effect of COF on shear-band orientations was controlled on average, considering dilatation using the dilatancy parameter ς (8) (Anand and Su, 2005), which treatment slightly increases the internal COF demonstrated in Fig. 3.

The remaining model parameters were calibrated to the stress vs. strain data using calculations in a single material point assumed to be representative for whole specimens, because the specimens showed virtually homogeneous deformation behavior during softening (Anand and Su, 2005) and yet during re-hardening, when the most ductile compositions were applied. Because the simulations times at one material point take up a very short time, an optimization method, such as least squares fitting, was not necessary for the calibration, and the parameters were rapidly determined after a few iterations. Details of the numerical calculations are discussed in Appendix B.

The two internal variables φ (average free volume in the micro-/macro-level) and s (average resistance to plastic flow) depending on φ include the plasticity parameters and define the observed hardening-softening behavior, as illustrated in Fig. 2(d). The evolution of φ (8) depends on the parameters g_0, φ_{cv}, and g_1, where φ_{cv} is the saturation value or the upper limit of φ, and g_0 and g_1 are used to define the softening characteristic due to SB. The evolution of s (12) depends on the parameters h_{T}, $\hat{h}_0$, $\hat{s}_0$, h_{B}, b, $\hat{s}_{cv}$ and q, where $\hat{s}_0$ is used to define the yield strength σ_y. The initial values of the key parameters $\hat{s}_{cv}$, g_0, and φ_{cv} were concluded from the evolution equations of s and φ using the closest literature (Anand and Su, 2005; Henann and Anand, 2009). The s_{T} in (12) was modeled following the celebrated Maxwell model for relaxation as

$$\dot{\gamma}^{\mathrm{p}}{}_{\mathrm{T}} = E^{-1}{}_{\mathrm{T}}\dot{s}_{\mathrm{T}} + \eta^{-1}{}_{\mathrm{T}}s_{\mathrm{T}}$$

where $\dot{\gamma}^{\mathrm{p}}{}_{\mathrm{T}}$ represents the corresponding plastic shear strain rate for s_{T}, and E_{T} and η_{T} are the stiffness and viscosity parameters in a nanoscopic region including multitude of STZs. During relaxation, $\dot{\gamma}^{\mathrm{p}}{}_{\mathrm{T}}$ is regarded as a unique constant in each nanoscopic region (under quasi-static loads) in which case the derivative $\mathrm{d}\dot{\gamma}^{\mathrm{p}}{}_{\mathrm{T}}/\mathrm{d}l_{\mathrm{T}}$ (l_{T} is the dimension of the region) vanishes. Using the relations $\mathrm{d}s_{\mathrm{T}} = \dot{s}_{\mathrm{T}}\mathrm{d}t$ and $\mathrm{d}t = \mathrm{d}l_{\mathrm{T}}/\dot{l}_{\mathrm{T}}$, one obtains $\mathrm{d}\dot{s}_{\mathrm{T}}/\dot{s}_{\mathrm{T}} = -T^{-1}{}_{\mathrm{T}}\mathrm{d}l_{\mathrm{T}}/\dot{l}_{\mathrm{T}}$, where $T_{\mathrm{T}} = \eta_{\mathrm{T}}/E_{\mathrm{T}}$ is the relaxation time within the nanoscopic region. Using the initial condition $\dot{s}_{\mathrm{T}}(\bar{t} = 0) = \dot{s}_{\mathrm{T},0} < 0$ (when $\gamma^{\mathrm{p}}{}_{\mathrm{T}}(\bar{t} = 0) = 0$ and $\bar{\epsilon}^{\mathrm{p}}(\bar{t} = 0) = 0$, cf. Fig. 2(c)) for hardening, the integration results in $\dot{s}_{\mathrm{T}} = \dot{s}_{\mathrm{T},0}\exp(-T^{-1}{}_{\mathrm{T}}l_{\mathrm{T}}/\dot{l}_{\mathrm{T}})$ ($\dot{l}_{\mathrm{T}}$ is constant in accordance with $\dot{\gamma}^{\mathrm{p}}{}_{\mathrm{T}}$). Considering $l_{\mathrm{T}}/\dot{l}_{\mathrm{T}} = t - \bar{t}$, the time integration results in $s_{\mathrm{T}} = -\dot{s}_{\mathrm{T},0}T_{\mathrm{T}}\exp(-T^{-1}{}_{\mathrm{T}}l_{\mathrm{T}}/\dot{l}_{\mathrm{T}})$. The transitions from nano- to macro-level were taken to be $T_{\mathrm{T}} \to \bar{T} = \eta/E$ and $T^{-1}{}_{\mathrm{T}}l_{\mathrm{T}}/\dot{l}_{\mathrm{T}} \to \bar{T}^{-1}\tilde{C}(\bar{\epsilon}^{\mathrm{p}}/\bar{\dot{\epsilon}}^{\mathrm{p}})^q$, where $\bar{T}$ and η are the macroscopic relaxation time and viscosity, $q > 1$ and $\tilde{C}$ are parameters, and $\bar{\dot{\epsilon}}^{\mathrm{p}}$ is taken to be the mean value of $\dot{\epsilon}^{\mathrm{p}}$ under quasi-static loads (limited to ~0.015 /s; higher values $\dot{\epsilon}^{\mathrm{p}} > 0.03$ /s cause transition from ductile to brittle). Obviously $\bar{T}$ of the macroscopic region is magnitudes greater than T_{T}'s of its nanoscopic regions and is a sum of T_{T}'s (T_{T}'s occur partially consecutively). Finally, $h_{\mathrm{T}} = \tilde{C}/(\bar{T}(\bar{\dot{\epsilon}}^{\mathrm{p}})^q)$ and $\hat{h}_0 = -\dot{s}_{\mathrm{T},0}\bar{T}$. Using $\tilde{C} = 1\ \mathrm{s}^{1-q}$, $q = 4$, $\dot{s}_{\mathrm{T},0} =\sim -0.5$ MPa/s, and reasonable values of E, η ($\eta =\sim 1.5 \cdot 10^6$ GPas Mukherjee et al., 2004) one obtains, after few iterations, $h_{\mathrm{T}} = 800$ and $\hat{h}_0 = 11$ GPa.

The parameters $h_{\mathrm{B}} > 1$ and b are used to refine softening behavior, where b can be estimated from (12) when $\dot{s} = 0$ before the stress drop ($\epsilon = \epsilon_{0.2} \approx 0.2$):

$$b = \frac{s_{0.2} - \hat{s}_{cv}}{\hat{s}_{cv}(\varphi_{cv} - \varphi(\epsilon_{0.2}))},\ s_{0.2} = s(\epsilon \approx 0.2).$$

The variables φ and s are shown in Fig. 2(a)–(b). It appears that $\hat{s}_{cv}$ is close to $\hat{s}_0$ and $s(\epsilon \approx 0.2)$ is approximately $1.2\hat{s}_0$.

The rate of shearing deformation (15) in each slip plane depends on the parameters k_1 (shear stressing) and k_2 (normal stressing). It was assumed that k_2 is an order of magnitude greater than k_1 (because k_2 is multiplied by μ_c), and k_2 is around unity (Henann and Anand, 2009). Subsequently, their values were quickly found after a few iterations. Because $k_2\mu_c\sigma^{\mathrm{k}}$ is almost equal to $-k_1\tau^{\mathrm{k}}$ in (15) under uniaxial loads, the simple evolution of shearing deformation in each slip plane

$$\dot{\gamma}^{\mathrm{p}}{}_{\mathrm{k}} = \dot{\gamma}_0(\tilde{\tau}/s)^{(1/m)}$$

can be applied for the model calibration.

Finally, the initial hardening modulus C_{R} (~20 MPa, cf. Fig. 2(d)), c_1, and c, just in that order, were determined for the hardening (21) at extremely large strains. The parameters c and c_1 were found after few iterations using the constraints $c < c_1 \gg 1$ (a magnitude greater than unity) and $\exp(-c(\lambda^{\mathrm{p}} - 1))/\lambda^{\mathrm{p},\alpha} \sim 1$ during hardening.

The constitutive model parameters are listed in Table 3. The total number of parameters needed to model complex deformation behavior of BMGs is 20. This number is relatively low compared to those of the previous constitutive models (Han et al., 2021) and the nanoscale models based on the dissipation energy (Zhou et al., 2018). Moreover, many quantities required in the nanoscale models are difficult to measure, and nanoscale models are insufficient for investigating macroscopic objects.

Table 3
Constitutive model parameters for the Zr-based BMGs used. The value of the Young's modulus E and the plasticity model parameters $\hat{s}_{sv}$, $\hat{s}_0$, and $\hat{h}_0$ depend on the chemical composition (see Appendix A), and the given values E, s_{sv}, s_0, and h_0 are for $Zr_{65}Cu_{15}Ni_{10}Al_{10}$. The initial free volume φ_0 (in macro-level) is considered to be zero.

Elastic parameters									
Parameter	E	ν	μ_c						
Unit	GPa								
Value	19.3	0.35	0.04						
Viscoplastic parameters									
Parameter	$\dot{\gamma}_0$	m	g_0	φ_{cv}	h_0	b	s_{cv}	s_0	
Unit	1/s				GPa		MPa	MPa	
Value	2E−4	0.05	0.003	0.005	11	55	954	980	
Parameter	h_T	h_B	k_1	k_2	g_1	q	C_R	c	c_1
Unit							MPa		
Value	800	1.4	0.15	5.0	4,000	4.0	20	13.2	24.0

4. Results and discussion

4.1. Influence of the chemical composition

The elastic deformation, elastic limit, and subsequent hardening-softening behavior strongly depended on the chemical composition (Wu et al., 2008; Fan et al., 2016). The following Zr-based BMGs were compared: (i) $Zr_{65}Cu_{15}Ni_{10}Al_{10}$, (ii) $Zr_{57}Cu_{20}Ni_8Al_{10}Ti_5$ (Fan et al., 2016), (iii) $Zr_{48}Cu_{45}Al_7$ (Wu et al., 2008), (iv) $Zr_{65}Cu_{18}Ni_7Al_{10}$ (Zhou et al., 2018), (v) $Zr_{52.5}Cu_{17.8}Ni_{14.5}Al_{10}Ti_5$, and (vi) $Zr_{40}Ti_{25}Cu_8Be_{27}$. The results for the compositions (ii)–(iv) were taken from the literature. The ductility of the first composition material (i) improved with a large Zr content and a lowered Cu content. The ductility of the compositions (v) and (vi) improved with Ti and/or Be.

The strain rates applied for the comparison varied between 0.0001 /s and 0.003 /s, see Table 2. However, the effect of strain rate, especially in this range, was small, cf. Fig. 3(left). The specimens consisting of the compositions (i), (ii), (v), and (vi) (low Cu content) were manufactured by suction casting under similar conditions, and the specimens consisting of the compositions (iii) (high Cu content) and (iv) (low content ratio Ni/Al) were manufactured by injection molding under equivalent conditions. It was assumed that the effect of the manufacturing method per se, with regards to the chemical composition, on the macroscopic deformation behavior near RT is small. However, the manufacturing details, especially those affecting crystallization of the alloy ingot, were crucial as discussed subsequently in Section 4.2.

When the Cu content was small (compositions (i), (ii), (v), (vi), see Table 2), hardening occurs ($\sigma_y < \sigma_c$), see Fig. 7. In the compositions (iii) and (iv), when the Cu content was large or the content ratio Ni/Al was low (without Ti or Be), respectively, the material shows pure softening ($\sigma_y > \sigma_c$) and undergoes final failure without hardening, see Fig. 7(a). The re-hardening after softening, when occurred in compositions (i) and (v–vi) showing superior ductility, did not appear to be sensitive to the chemical compositions used, that is, the re-hardening responses (hardening modules) of the different compositions shown in Figs. 7(b–d) (also in Figs. 9(a–b)) are similar. The results in Fig. 7 purport the capability of the model to reproduce different hardening and softening behaviors of different chemical compositions (through Eqs. (A.1)–(A.3) in Appendix A).

At high enough (compressive) strain rate, a transition from stable deformation to unstable deformation occurs, making the material behavior more brittle as illustrated in Fig. 7(b) for the composition (v). The two extremes of the test results at each strain rate are displayed, and a large deviation of the test results occurs when the Zr content is reduced and the content is replaced by Cu and Ni. As a result, this material behavior is the most challenging to test and can only be predicted on average. Unstable deformation and reduced ductility have been shown to be due to (1) the material's susceptibility to multiple SBs (slip planes) (Qiao et al., 2016) and to (2) subsequent fracture surfaces wherein SB patterns are different from vein-like and rippled patterns, which characteristic may be partially due to a local temperature rise, see Zhu et al. (2021), Zhou et al. (2018). This indicates that the applied energy is not fully dissipated by localized SBs when unstable deformation occurs (Zhou et al., 2018). These two characteristics (1–2) partially explain the differences in ductility between the different compositions, but the whole picture remains still uncertain. A conclusion so far is that an increase in Cu content at the expense of a decrease in Zu content increases the material's susceptibility to multiple SBs and their slip planes reducing ductility. Concurrent formation (diffusion) of multiple SBs is crucial for the plasticity improvement in metallic glasses (Du et al., 2009), and this issue is subsequently discussed in Section 4.2. The formation of SBs per se during the first hardening is known from the previous literature (Schuh et al., 2007; Park, 2015; Kruzic, 2016): nucleation and coalescence of nanovoids (free volume) to form of SBs. Moreover, the composition (v) shows a notable reduction of the yield strength with increasing strain rate. This unstable deformation was modeled using the damage, discussed in Appendix C.

Finally, very ductile responses of the last composition (vi) at the two different strain rates are shown in Fig. 7(c–d). It is noteworthy that softening of this composition, when Ni, Al, and a part of Zr were replaced by Ti and Be, is sensitive to the strain rate; no stress drop occurs at the lowest strain rate, whereas a stress drop may occur at the higher strain rate.

The influence of the compositions on the yield strength σ_y and yield strain is further illustrated in Fig. 8(a) (at the strain rates informed in Table 2), where the two clusters are observed. The BMGs in the second cluster are most ductile (incl. Ti and/or Be). When replacing Ti and/or Be essentially by Zr (composition (i)), the ductility is yet high compared to the compositions (ii)–(iv) (high Cu-content or low content ratio of Ni/Al). These results are also reflected in the σ_c shown in Fig. 8(b), although the deviation is larger. The ductility of the compositions in terms of the product of the ultimate strength, strain, and strain rate, $\sigma_u \epsilon_u \dot{\epsilon}$ is compared in Fig. 8(c), showing the compositions (i) and (vi) are by far the most ductile.

4.2. Mechanical behavior of Zr_{65} $Cu_{15}Ni_{10}Al_{10}$

Monotonic loading

The composition (i) uniquely showed a fair softening followed by re-hardening at extremely large strains, and it was the most stable at the observed strain rates; thereby it is forth investigating further. Both the measured and model responses show the deformation behavior characterized first by a low work hardening (Wang et al., 2018; Zhou et al., 2018) and then by a rapid softening, see Fig. 9(a–b). During the hardening ($\sigma_y < \sigma_c$), the serrated flow typical of BMGs occurs, which is due to the formation of multiple SBs (Brechtl et al., 2020). However, the amplitude of the serrated curve reduces or even disappears with an increase in the strain rate (Zhu et al., 2021). The hardening has been reported to be followed by the origination of SBs generated by a multitude of STZs as described above, and the greater the density of SBs, the greater is the ductility and plastic strain, and the characteristic that the density of SBs increases with reducing strain rates holds (Zhu et al., 2021). The SB density in many Zr-based alloys can be phenomenologically described by a simple law $\rho_{sb} = C\sqrt{\epsilon^p}$, where C (about 0.085 μm^{-1}) is a material parameter and ϵ^p is the plastic strain Kruzic (2016). Using this law, our compression measurements showed growth of $\rho_{sb} = 0.015\ \mu m^{-1}$ solely during softening ($\Delta\epsilon^p = 0.03$, see Figs. 2(b, d)), whereas (Yanga et al., 2004) (Fig. 7) showed that $\rho_{sb} = 0.007\ \mu m^{-1}$ (activation of numbers of SBs divided by the gauge length of the specimen, 9525 μm) at $\epsilon^p = 0.03$ is small in tension.

The effect of the applied strain rates $\dot{\epsilon} = 0.003...0.033$ /s on the initial elastic response and subsequent hardening stage is small, i.e., the reduction (and deviation) of the yield strengths σ_y and σ_c is small.

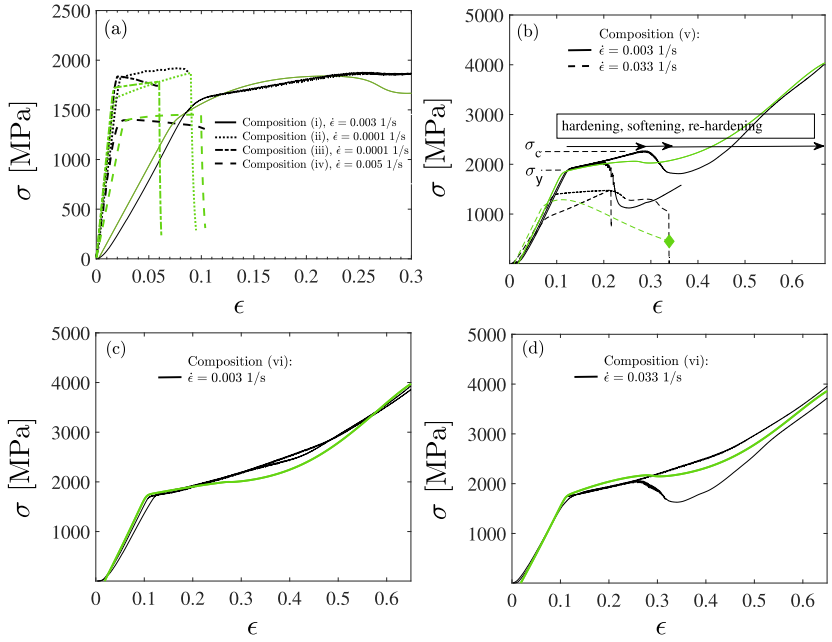

Fig. 7. Predicted (green) and measured (black) stress vs. strain responses for different chemical compositions (i)–(iv) (a). Predicted (green) and measured (black) responses of the composition (v) (b). Two extreme test results for both strain rates are shown. Damage at $\dot{\epsilon} = 0.033$ /s develops until interruption (green diamond marker). Predicted (green) and measured (black) stress vs. strain responses of the composition (vi) at $\dot{\epsilon} = 0.003$ /s (c) and $\dot{\epsilon} = 0.033$ /s (d). (For interpretation of the references to color in this figure legend, the reader is referred to the web version of this article.)

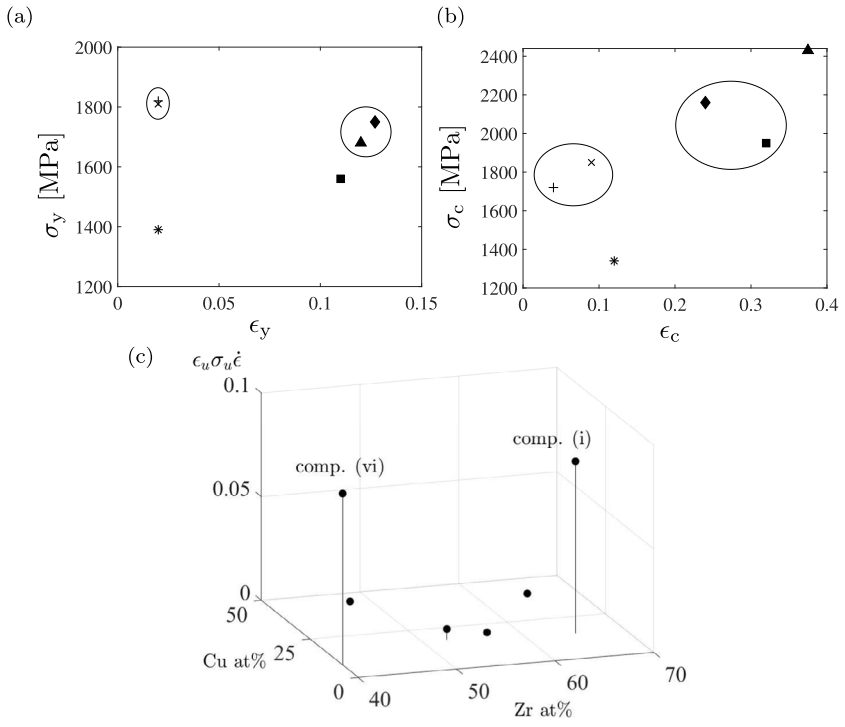

Fig. 8. A chart representing the yield strength vs. yield strain for different chemical compositions: (i) (marker ■), (ii) (marker X), (iii) (marker +), (iv) (marker ∗), (v) (marker ♦), and (vi) (marker ▲) (a). Data represent mean values. Two observed clusters are highlighted by ellipses. Corresponding upper yield strengths vs. strains (b). Ductility in terms of the product $\sigma_u \epsilon_u \dot{\epsilon}$ (c). The compositions are identified in Table 2.

In Ravichandran and Johnson (2003) was showed that the quasi-static strain rate does not have a marked effect on the yield stress of Zr-based BMGs at temperatures below 600 K (well below the glass transition). This indicates that the SBs on the fracture sides do not easily increase at low strain rates and temperatures (Zhu et al., 2021). In contrast, the strain rate has a notable effect on the rapid softening stage when slip planes emerge (Zhu et al., 2021), which characteristic explains the sensitivity and deviation of the measured results. At the end of softening, under a heavy compression load, the development of large SBs rapidly reduces because yet more dissipation energy is required for SB, and the material response then is capable to show re-hardening at extremely large strains.

At the highest strain rate $\dot{\epsilon} = 0.333$ /s, the material shows a distinct reduction of the yield strength, Fig. 9(a), which unstable deformation

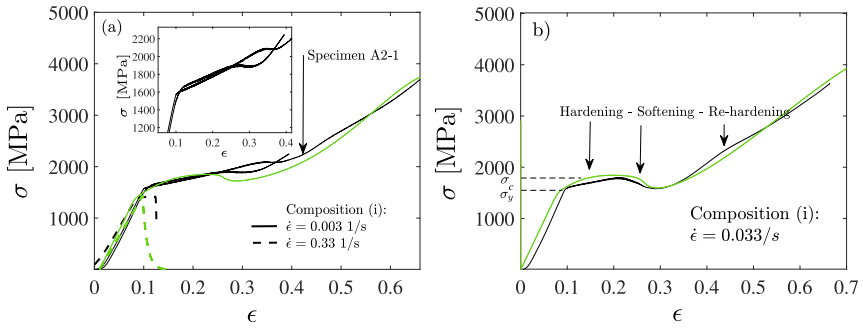

Fig. 9. Predicted (green) and measured (black) stress vs. strain responses of the composition (i) under the monotonic loads, when $\dot{\epsilon} = 0.003$ /s, $\dot{\epsilon} = 0.33$ /s (a), and $\dot{\epsilon} = 0.033$ /s (b). The inset shows the serrated flow before the re-hardening (a).

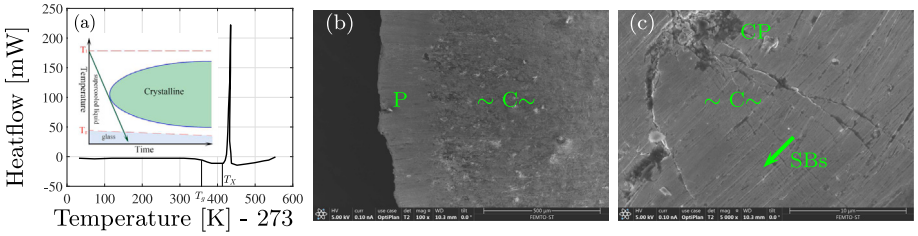

Fig. 10. DSC curve of $Zr_{65}Cu_{15}Ni_{10}Al_{10}$ with the heating rate of 3 K/min (a). The inset demonstrates a TTT diagram for the cooling rate for crystallization. SEM image (top view of the specimen A2-1 for $Zr_{65}Cu_{15}Ni_{10}Al_{10}$) before testing showing the degree of crystallization (dark spots) in the core (C) (b). Abbreviation P means the periphery of the specimen. SBs (thin diagonal lines) and the crossing microcracks around crystallized particles (CP) (dark appearance) in the C after the test (c).

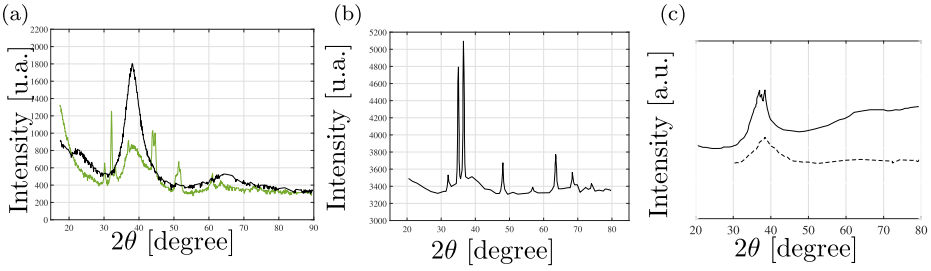

Fig. 11. XRD patterns of the $Zr_{65}Cu_{15}Ni_{10}Al_{10}$ BMG (as-cast state) in the periphery (black) and the core (green) regions (a). A comparative XRD pattern of CuZrAl glassy matrix composite (Cardinal et al., 2018) (b). Main characteristics of the XRD patterns (in arbitrary units) for the compositions (iii) (dashed) and (iv) (solid) extracted from (Wu et al., 2008) and Zhou et al. (2018), respectively (c). (For interpretation of the references to color in this figure legend, the reader is referred to the web version of this article.)

was modeled by the damage, see Appendix C. The experimental response reveals that the strain is then $\epsilon = 0.08$, that is, plastic strain is virtually zero, and the predicted free volume $\varphi = 0.0004$ represents the threshold of damage, after which the formation of multiple primary SBs leads to cracking and rupture of the specimen.

The model results show a good fit to the measured data for monotonic loadings; the initial elastic response, hardening, softening, and subsequent re-hardening are all accurately predicted, as depicted in Fig. 9(a–b).

Influence of crystallization

The phase separation during casting resulted in some crystallization, cf. Wang et al. (2018). The DSC result in Fig. 10(a) shows that the glass transition temperature T_g and crystallization temperature T_X were approximately 645 K and 690 K, respectively, and the super liquid region (SLR) defined by $T_X - T_g$ was rather limited, 45 K. Moreover, the value of T_X being far below the liquidus temperature T_l (~ 1100 K) achieved in the casting indicates that some crystallization occurred in the specimens (on the time–temperature-transformation (TTT) diagram of BMGs, the slope of the arrow indicating the cooling rate pierced the nose of the region for crystallization).

The SEM fractograph in Fig. 10(b) evidences the crystallization. The degree of the crystallization (DC) was practically reduced to zero in the periphery of the specimen (the 'near-surface region') during the casting in cooled copper mold (due to more rapid cooling compared to core region). This inhomogeneity of crystallization is a characteristic of casting methods (Fu et al., 2020). The XRD measurements in Fig. 11(a) confirm this: a broad diffraction peak occurs in the periphery, whereas sharp diffraction peaks at $2\theta = 32°$, 44°, and 52° are present in the core, that is, a crystalline phase can be detected. The DC (the ratio of the areas of the crystalline peaks to the total area) in the core was observed to be approximately 5%.

Crystalline Zr having the highest melting point (2100 K) in the ingot was expected to form small crystalline particles. The high Zr content has been shown to increase crystallization also in powder-based BMGCs (Cardinal et al., 2018); Fig. 11(b) shows high diffraction peaks of an ex-situ glassy matrix composite (a glassy $Cu_{50}Zr_{45}Al_5$ powder mixed with 50 vol% of pure crystalline Zr powder), and the height of peaks and ductility of the composite increase with the amount of crystalline Zr (Cardinal et al., 2018). Hui et al. Wang et al. (2018) concluded that crystalline particles in a Zr-based BMG consisted of CuZr-crystals (dark gray metal-composition in relation to the light BMG as it appears in Fig. 10(b–d)). The performed XRD measurements confirmed that the Zr content of the crystallized regions is high (up to 99%). The XRD results also showed that a marked portion of the glassy material ~ 35% consists of Cu-Al including light Al up to 82%.

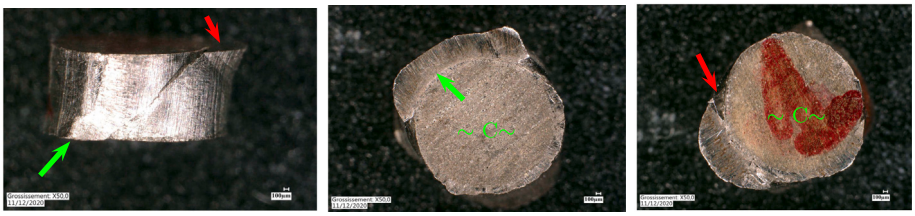

Fig. 12. Visualization of the shape of the ruptured specimens (the non-contact metrology by the Werth video-check machine) after the monotonic loading (specimen A2-1). The side, bottom, and top views are presented. The specimens show crack transection (highlighted by the arrows) and failure into flakes, cf. Zhou et al. (2018).

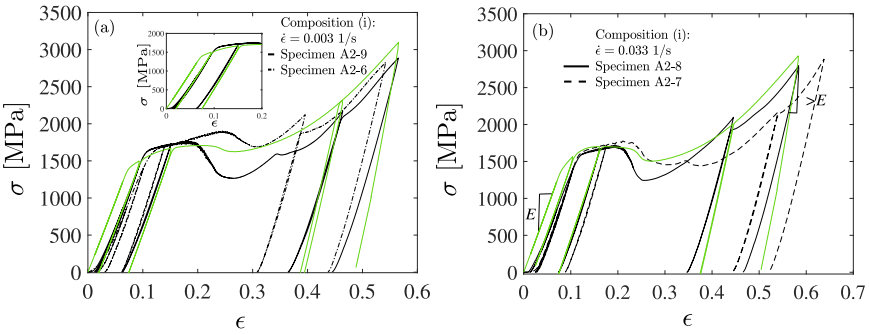

Fig. 13. Predicted (green) and measured (black) stress vs. strain responses under the PRLs when $\dot{\epsilon} = 0.003$ /s (a) and $\dot{\epsilon} = 0.033$ /s (b). The inset shows the initial model response and data (a). The unloadings in the tests were started when stresses of 850 (elastic), 1450 (near to the yield stress), 1700, 2100, and 2800 MPa had been reached (in the most brittle case, the last unloading was not achieved). (For interpretation of the references to color in this figure legend, the reader is referred to the web version of this article.)

Fig. 10(c) shows that small crystallized particles (nanocrystals) and their clusters (around 1 μm) in the core efficiently block the extension of SBs and microcracks and thereby increase their diffusion and improve ductility. This characteristic was considered as the underlying mechanism of re-hardening and extreme plasticity, and it explains the superior ductility over the other compositions (ii)–(iv); no sharp diffraction peaks indicating crystallization was observed in compositions (ii)–(iv), see Fig. 11(c) and Fan et al. (2016), Wu et al. (2008), Zhou et al. (2018).

The ruptured shapes showed failure surfaces which occur at an angle of approximately 45° to the loading direction, referring to concentrated SB leading to a sudden cracking and flaking of the specimens (Kruzic, 2016; Zhou et al., 2021; Zhu et al., 2021; Wu et al., 2008; Shahabi et al., 2015; Anand and Su, 2005). Comparison of Figs. 10(b) and 12 reveals that the most significant failure surface occurs in the glassy periphery or between the periphery and core of the specimen, whereas sufficiently crystallized core has been remained intact, i.e., sufficient, small crystallization (DC~ 5%) improves ductility.

PRL-tests

Two extremes of the test results are displayed in Fig. 13. In the modeling, the initiation of load removal follows the measured reference strain data, i.e., the model was evaluated based on the observed stress. The reference strain data was extracted from the data which shows the second last unloading around $\epsilon = 0.4$ (A2-9 and A2-8 for the strain rates 0.003 /s and 0.033 /s, respectively). The first two unloading cycles (almost elastic) do not appear to affect the yielding and hardening, and the model accurately predicts the first three unloading loops and hardening. During anomalous softening, the data show notable deviation and the model predicts an average of the data. In addition, the model predicts hardening at very large strains (from 0.3) fairly well, also after unloading and reloading. Notably, the stress vs. strain responses immediately after the reloadings coincide with the primary curve, which virtually overlaps with the monotonic curve, as depicted in Fig. 9. Only relatively small stress drops after the reloadings are observed in the intermediate strain regime, that is, between 0.35 and 0.45. This desired property appears to be a characteristic of glassy metals and differs from glassy plastics, which show a notable peak stress after reloading (Holopainen, 2013, 2014).

The last two measured unloading responses at very large strains purport some nonlinear behavior, whereas the model predicted almost linear unloading responses. Such nonlinear behavior does not occur in crystalline metals, and volume expansion in the plastic zones (plastic dilatation) can be expected to give rise to an elevated stiffness during initial unloading (Kruzic, 2016), as demonstrated in Fig. 13(b). The nonlinear unloading response also resembles the unloading behavior of glassy polymers, showing a volume expansion (Holopainen, 2013). It will be shown subsequently that the nonlinearity of the unloading response is a sensitive function of the free volume (within SBs) and damage.

Influence of geometrical imperfections

Under some PRL-tests, the stress response showed a small stress drop during hardening once a strain of 0.3 was passed, Fig. 13. Because the additional stress drop did not appear in all tests (especially in those of the monotonic shown in Fig. 9), the matter does not concern material's intrinsic behavior (e.g., cracking and abrupt deformation induced crystallization, Wang et al., 2018), but preferably undesired geometrical imperfections affecting undesired shape distortion as illustrated in Fig. 12. In Wu et al. (2008) and Fan et al. (2016), it was shown that a tilt angle of two degrees on the top surface (ψ in Fig. 14) affects a notable shearing and distortion of the compressed test specimens before rupture.

A small tilt angle between the top and bottom surfaces of the specimen and platens (observed to be less than $\psi < 1°$) was assumed to result in a high contact pressure around the upper right and lower left corners of the specimen. It was further assumed that the contact pressure increases the free volume and thereby, affects dilatation due to SB leading to microcracking. This assumption was motivated by cold working manufacturing methods, which show an increase of the free volume and microcracking in BMGs under compression (Kruzic, 2016). It is also known that a large enough free-volume creation promotes SB concentration and affects microcracking followed by macrocracking (Kruzic, 2016; Han et al., 2021; Zhao et al., 2019; Rao et al., 2019).

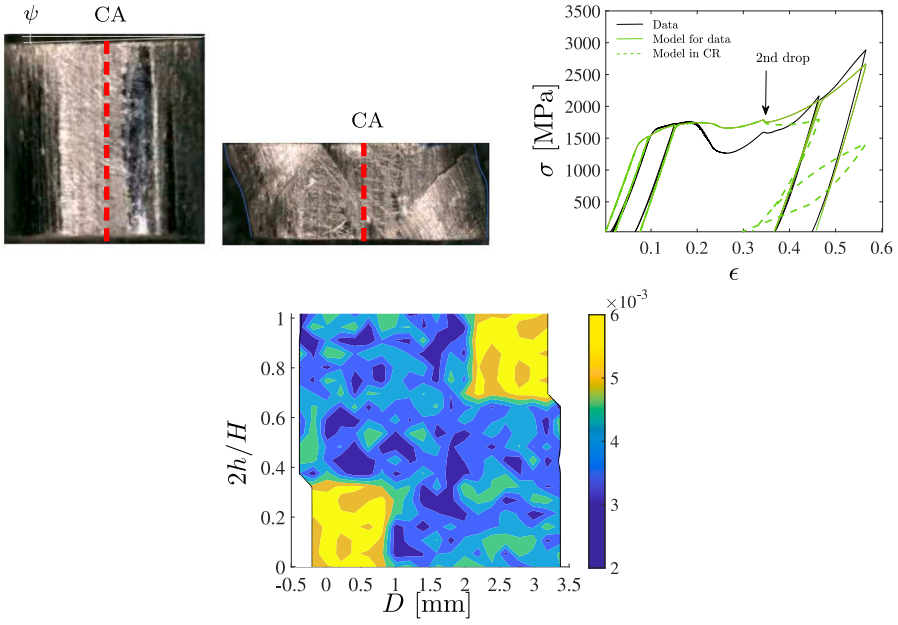

Fig. 14. Initial shape of the specimen (A2-9, composition (iv)) (top left). CA means the central axis. The initial measured tilt angle was $\psi < 1°$. The final shape of the specimen (the scale is accordance with the initial shape) after the PRL-test at $\dot{\epsilon} = 0.003$ /s (top middle). The machine $\sigma - \epsilon$ response (black curve is data and green is the prediction) and the predicted $\sigma - \epsilon$ response (green dashed, $\varphi_{cv} = 0.006$) in the corner region (CR) (top right). The final shape and the pattern of the free volume φ by the FEM simulation based on a random distribution of the limit φ_{cv} (bottom). (For interpretation of the references to color in this figure legend, the reader is referred to the web version of this article.)

The model was implemented in a commercial finite element method (FEM) program using user material subroutine (UMAT). The rupture of the specimens into flakes, Qiu et al. (2012), was observed to be rapid, i.e., visible cracking and material inhomogeneity were observed just shortly before the rupture. Therefore, deformations features of microstructural changes in the compressed cylindrical specimens were revealed using two-dimensional plane-stress calculations in the representative middle plane of the specimen in which the out-of-plane shear deformations relative to the in-plane shear deformations were smallest (observed visually from the Werth video-check figures, cf. Fig. 12). The numerical integration procedure of the model is discussed in Appendix B.

A random distribution of φ_{cv} was enabled in the range of 0,0025...0,005 overall, and between 0,005...0,006 in the corner regions of the rectangular plane (representing the glassy periphery in Fig. 10(b)). The influence of increasing free volume affecting microcracking was on averagely described by the material damage, D, see Appendix C. The damage describing the ad-hoc macroscopic stress drop during hardening was triggered when the free volume exceeded the limit $\bar{\varphi} = 0.005$ and the strain $\epsilon = 0.34$ was reached. The constant value $\hat{g}_0 = 30 g_0 < g_0{}^{u}$ in (10) for free volume (9) was applied in this stage ($\epsilon > 0.34$, $\varphi > 0.005$).

Due to the damage in the corner regions, the ability of the material to withstand the load is reduced, and the overall load (measured by the machine in the tests) reduces (under the displacement control) showing a drop in the stress response during hardening, see Fig. 14(top right). The figure also shows that the elastic stiffness (Young's modulus) and stress in the corner regions are substantially reduced as the free volume has increased ($\varphi_{cv} = 0.006$) and damage has emerged. It is noteworthy that the unloading response is nonlinear after the increased free volume and damage, and it means that the nonlinearity is a sensitive function of the free volume (causing dilatation) and damage (suppressing dilatation) (Kruzic, 2016; Luo et al., 2019; Suryanarayana, 2012). The predicted material behavior shows full reversibility and increased plastic dissipation (area of the loading loop), which suppresses the deformation (residual strain) and dilatation after the load removal.

Fig. 14(bottom) shows the simulated distribution of the free volume ($\varphi = \varphi_{cv}$) and the final shape of the specimen at the end of the test, before rupture. The free volume, and consequently damage, developed inhomogeneously, and their high concentration in the corner regions describes the transformation from ductile deformation behavior to more brittle. Then the deformability, including the radial component, was suppressed in the corner regions, cf. Fig. 14(top right), affecting a notable distortion similar to that observed in the test specimens, cf. Fig. 14(top middle). Interestingly, the central axis of the specimens did not pivot during the tests, that is, the shape distortion cannot be explained by shear deformation owing to sliding between the specimen and machine platens. Therefore, according to the observed and simulated results, we can conclude at affirmative answers that the final shape distortion of the specimens was due to a small tilt angle, and the shape distortion was further escalated by the free volume affecting damage.

5. Conclusion

Ductility could be significantly improved through chemical composition change (increased Zr, Ti, and Be content relative to Cu content) and allowance of the formation of sufficiently low degree of crystallization, DC~ 5%, i.e., the highest GFA was not optimal for ductility. The lower the T_g, the more ductile the composition, and the most ductile compositions $Zr_{40}Ti_{25}Cu_8Be_{27}$ and $Zr_{65}Cu_{15}Ni_{10}Al_{10}$ showed strains up to 70% yet at a strain rate of almost 0.04 /s. Their ultimate ductility, in terms of the product $\sigma_u \epsilon_u \dot{\epsilon}$ was 1500% higher than previous state-of-the-art results.

With the most ductile BMGs tested, a particular deformation behavior, that is, the hardening-softening-re-hardening was noticed. Contrast to yielding and softening, re-hardening was not sensitive to the chemical composition.

Based on the data, a thermodynamically relevant elastic-viscoplastic constitutive model was proposed to simulate explicitly the influence of the chemical composition, DC, deformation history, average shear resistance to the plastic flow, and the average free volume on the macroscopic deformation behavior. It was concluded that the high contact pressure between the platens and the specimen (localized due to a tilt angle) increases the free volume (representing local dilatation), which then causes damage reducing significantly plastic dilatation

and deformability and explaining the observed nonlinear unloading responses and distortion of the compressed specimens.

In summary, ductility was found to be critical to chemical composition, crystallization, and the deformation rate and thus, the success of BMGs in solid-state processing and engineering applications (fatigue resistance). The results suggest that with regards to ductility, the shortcomings of BMGs against ductile BMGCs (consisting of granulates) and crystalline metals can be overcome. Quantification of the crystallite distribution (mean spacing and size) and its simulation are definitely one of the research matters in future.

CRediT authorship contribution statement

T. Barriere: Designed the experiments, Arranged the testing facilities, Wrote the majority of the experimental section, Contributed the literature review and analyzed the results. **X. Gabrion:** Designed the experiments, Performed the experiments, Contributed the literature review and analyzed the results. **S. Holopainen:** Designed the experiments, Proposed the model, Performed the simulations, Wrote the majority of the paper, Contributed the literature review and analyzed the results. **N. Niang:** Performed the Werth video-check and DSC measurements, Wrote the majority of the experimental section, Contributed the literature review and analyzed the results. **J-M. Pelletier:** Provided the material, Wrote the majority of the experimental section, Contributed the literature review and analyzed the results.

Declaration of competing interest

The authors declare that they have no known competing financial interests or personal relationships that could have appeared to influence the work reported in this paper.

Data availability

Data will be made available on request.

Acknowledgments

The research was supported by the EIPHI Graduate School (contract ANR-17-EURE-0002) including its experimental facilities (cutting of test specimens, Werth video-check, X-ray tomography, DSC, and optical 3D metrology). The authors are grateful to MIFHySTO technological platform for the use of equipments and to J.C QIAO (NWPU, Xi'an, China) for providing the materials. We also thank Dr. S. Carbillet for the additional tests on different materials and Prof. F. Bernard for the XRD-tests.

Appendix A. Influence of the chemical composition on yielding and softening

A comparison of different BMGs shows that the low Zr content and high Cu content increase the yield stress and decrease the yield strain, because they promote the concentration of SBs and free volume within the SBs, and affect then brittleness and a premature local failure (Wu et al., 2008; Fan et al., 2016; Zhou et al., 2018). The tests also evidenced that the ductility increases with sufficiently high Ti- and Be-contents. Therefore, softening is influenced by the chemical composition via the asymptotic limit $\hat{s}_{cv}$ of S as follows:

$$\hat{s}_{cv} = (1 - \xi_{Cu} A_{Cu})(1 + \xi_{Zr}(0.65 - A_{Zr}))(1 - (\xi_{\mathrm{Ti}} A_{\mathrm{Ti}} + \xi_{\mathrm{Be}} A_{\mathrm{Be}}))s_{cv}, \quad \text{(A.1)}$$

where A_{Zr}, A_{Cu}, A_{Ti}, and A_{Be} are the contents of Zr, Cu, Ti, and Be (the nominal atomic percentage at% in decimal digits), and s_{cv} is the corresponding parameter value for the reference material, $Zr_{65}Cu_{15}Ni_{10}Al_{10}$. The effect of s_{cv} towards increasing σ_c is depicted in Fig. 2(d). The Ti and Be contents compensate for the increase in $\hat{s}_{cv}$ when the Zr and Cu contents are low. Comparing the first four materials in Table 2 led to fixed values of $\xi_{Cu} = 0.78$ and $\xi_{Zr} = 2.5$. These values were determined after the model calibration for the reference material, as discussed in Section 3.2. Similarly, comparing the first and the last two materials in Table 2 led to fixed values of $\xi_{\mathrm{Ti}} = 1.0$ and $\xi_{\mathrm{Be}} = 0.4$.

Moreover, the Zr content seemed to considerably reduce the yield stress, the effect of which is considered in the initial value of s as

$$\hat{s}_0 = (1 + \xi_{Zr0}(0.65 - A_{Zr}))(1 - \xi_{\mathrm{Ti}0} A_{\mathrm{Ti}})s_0, \quad \text{(A.2)}$$

where $\xi_{Zr0} = 1.5$ and $\xi_{\mathrm{Ti}0} = 0.25$ (based on the comparison of the first and the last two materials in Table 2), and s_0 is a specific parameter value for the reference material. The Ti content compensates for the increase in $\hat{s}_0$, when the Zr content is low (influence of Be was found to be low). The Ti and especially the Be content also reduce the softening (stress drop), which effect is modeled by reducing h_0 for the reference material as

$$\hat{h}_0 = (1 - (\xi_{\mathrm{Ti},h} A_{\mathrm{Ti}} + \xi_{\mathrm{Be},h} A_{\mathrm{Be}}))h_0, \quad \text{(A.3)}$$

where $\xi_{\mathrm{Ti},h} = 2.2$ and $\xi_{\mathrm{Be},h} = 1.0$. The reduced effects of h_0 on σ_c and subsequent softening are illustrated in Fig. 2(d).

The adjustment of yielding and softening through (A.1)–(A.3) for different chemical compositions is in line with previous research (Anand and Su, 2005; Zhou et al., 2018), which shows that the unstable deformation in the local softening region is governed by the energy dissipation through SB and sliding along slip systems accommodated by the stress, both of which are strongly affected by the chemical composition.

Appendix B. Calculation

The model was programmed by using the Intel® Fortran application. The numerical solution algorithm for the displacement-controlled loadings is based on the evolution of the plastic deformation (5). To define the stress-free intermediate configuration uniquely, the plastic spin in (5) was required to be zero, i.e., $\boldsymbol{L}^{\mathrm{p}} = \mathrm{sym}(\boldsymbol{L}^{\mathrm{p}}) = \boldsymbol{D}^{\mathrm{p}}$, cf. Anand and Su (2005) and Barriere et al. (2020). Calculations for the plane-stress conditions were based on the implicit integration of the following system of equations:

$$\begin{aligned}
&\boldsymbol{F}^{\mathrm{p}}(1,1) - \boldsymbol{F}^{\mathrm{p}}{}_{\mathrm{N}}(1,1) - \mathrm{d}t(\boldsymbol{D}^{\mathrm{p}}(1,1)\boldsymbol{F}^{\mathrm{p}}(1,1) + \boldsymbol{D}^{\mathrm{p}}(1,2)\boldsymbol{F}^{\mathrm{p}}(2,1)) = 0\\
&\boldsymbol{F}^{\mathrm{p}}(2,1) - \boldsymbol{F}^{\mathrm{p}}{}_{\mathrm{N}}(2,1) - \mathrm{d}t(\boldsymbol{D}^{\mathrm{p}}(2,1)\boldsymbol{F}^{\mathrm{p}}(1,1) + \boldsymbol{D}^{\mathrm{p}}(2,2)\boldsymbol{F}^{\mathrm{p}}(2,1)) = 0\\
&(s - s_{\mathrm{N}} - \dot{s}\mathrm{d}t)/s_0 = 0\\
&\varphi - \varphi_{\mathrm{N}} - \dot{\varphi}\mathrm{d}t = 0,
\end{aligned} \quad \text{(B.1)}$$

where the subscript N refers to the known state (the number of time increments) at the end of the previous step and $\boldsymbol{F}^{\mathrm{p}}(1,1) = \lambda^{\mathrm{p},1}$, where the index 1 refers to the axial direction of the specimens. A thin slice in the middle of the cylindrical specimen (the 1–2 plane) was modeled, where practically $\boldsymbol{\tau}(3,3) = \boldsymbol{\tau}(2,2) = \boldsymbol{\tau}(1,3) = \boldsymbol{\tau}(2,3) = 0$ (the slice where the observed out-of-plane shear deformations relative to the in-plane shear deformations are the smallest) and $\boldsymbol{F}^{\mathrm{p}}(1,3) = \boldsymbol{F}^{\mathrm{p}}(3,1) = \boldsymbol{F}^{\mathrm{p}}(2,3) = \boldsymbol{F}^{\mathrm{p}}(3,2) = 0$, and $\boldsymbol{F}^{\mathrm{p}}(1,2) = 0$. The plastic dilatation was allowed by the relaxed constraint $\boldsymbol{F}^{\mathrm{p}}(2,2) = \boldsymbol{F}^{\mathrm{p}}(3,3) = \sqrt{J^{\mathrm{p}}/\boldsymbol{F}^{\mathrm{p}}(1,1)}$, where

$$J^{\mathrm{p}} = \det(\boldsymbol{F}^{\mathrm{p}}) = \lambda^{\mathrm{p},1}\exp(-2\nu^{\mathrm{p}}\log(\lambda^{\mathrm{p},1})), \quad \text{(B.2)}$$

and the value $\nu^{\mathrm{p}} = \nu$ was based on a non-contact metrology to obtain the shape and dimensions of the final specimens.

Under the displacement control (used in the standard FEM applied), the total deformation gradient $\boldsymbol{F}$ is known, and the components of $\boldsymbol{F}^{\mathrm{e}}$ were solved from the decomposition (1) based on the updated values of $\boldsymbol{F}^{\mathrm{p}}$. The strain-rate-dependent time step used was $\Delta t = 0.05 \cdot 0.003/\dot{\varepsilon}$. A mesh consisting of 4-node bilinear planar elements was used (Zhao et al., 2020). The central axis (CA) of the specimen was fixed horizontally at both ends (the CA did not pivot during the tests), sliding between the platens and specimen was allowed, and the bottom platen was vertically fixed. The cohesion bands against the corner regions

shown in Fig. 14(bottom) were considered with four layers of triangular elements.

Based on the expression of stress (3), the treatment of the algorithmic tangent stiffness (ATS) tensor for the implicit finite element method, neglecting damage, is given by Holopainen and Wallin Holopainen and Wallin (2012). The damage development was not assumed to influence the global tangent stiffness, that is, once the plastic deformation and the internal constitutive variables φ and s have been solved, the damage D was calculated retrospectively. This assumption was based on our and previous experimental observations (Kruzic, 2016) that the damage representing solely and averagely (in micro/macro-level) the unstable deformation (formation of fracture surfaces and micro-cracks), shows notable values (and thus, inaccuracy in the calculations) just shortly before the rupture of the specimens.

Appendix C. Damage

The observed brittle deformation behavior, when occurred, was modeled by damage, D, which is governed by the reduction of the Young's modulus E according to $\mathrm{d}E = -KE$. The two material-dependent thresholds for damage must be attained: the threshold strain ϵ_{D} and threshold strain rate $\dot{\epsilon}_{\mathrm{D}}$. The coefficient $K > 0$, which can depend on the free volume, is a small enough function of these thresholds. The current Young's modulus is $\tilde{E} = (1-K)^{\mathrm{N}}E = (1-D)E$, i.e., damage is $D = 1-(1-K)^{\mathrm{N}}$, where N is the number of time increments; the damage evolution is based on the $[1-D]$ concept (Lemaitre and Chaboche, 1999). The damage growth, once the free volume evolves, is reducing, as shown in Fig. 2(a) (a constant value $K = 0.0015$ was simply used). This damage development obeys the activation of numbers of SBs as shown in Yanga et al. (2004, Fig. 7b). The sole purpose of the damage calculation here is to mimic the impaired load-bearing capacity of materials through the reduction of the Young's modulus and therefore a more advanced development work for microstructure-based damage has been left to the future.

In the model predictions shown in Figs. 7(a–b), damage was initiated when $\epsilon_{\mathrm{D}} = 0.060$ ($\varphi = 0.0007$, composition (iii)) and $\epsilon_{\mathrm{D}} = 0.095$ ($\varphi = 0.0009$, compositions (ii) and (iv)). The high value $K = 0.1$ was required for these relatively brittle compositions. The free-volume thresholds are mentioned because the free volume is an important factor in the transition from ductile stable deformation to unstable and brittle (Zhu et al., 2021; Zhou et al., 2018). The threshold strain $\epsilon_{\mathrm{D}} = 0.06$ was used at the higher strain rate $\dot{\epsilon} = 0.033$ /s for the composition (v), and the value $K = 0.0015$ used was magnitudes lower compared to the brittle compositions (ii)–(iv) indicating a much lower damage rate. In Fig. 9(a), $K = 0.02$ was used, and the strain threshold corresponds to $\varphi = 0.0004$. Damage in Fig. 14 was modeled as described above, but $K = \hat{K}(\varphi_{cv} - \varphi)/\varphi$ and $\hat{K} = 0.013$ were used.

References

Afonina, G.V., Mitrofanova, Yu. P., Kobelevb, N.P., Khonik, V.A., 2020. Shear modulus relaxation and thermal effects in a $Zr_{65}Cu_{15}Ni_{10}Al_{10}$ metallic glass after inhomogeneous plastic deformation. J. Exp. Theor. Phys. 131, 582–588.

Anand, L., Ames, N.M., 2006. On modeling the micro-indentation response of an amorphous polymer. Int. J. Plast. 22, 1123–1170.

Anand, L., Su, C., 2005. A theory for amorphous viscoplastic materials undergoing finite deformations, with application to metallic glasses. J. Mech. Phys. Solids 53, 1362–1396.

Barriere, T., Gabrion, X., Holopainen, S., Jokinen, J., 2020. Testing and analysis of solid polymers under large monotonic and long-term cyclic deformation. Int. J. Plast. 135, 102781.

Berdichevsky, V., 2014. Overcoming paradoxes of Drucker-Prager theory for unconsolidated granular matter. Internat. J. Engrg. Sci. 83, 174–186.

Brechtl, J., Xie, X., Wang, Z., Qiao, J.W., Liaw, P.K., 2020. Complexity analysis of serrated flows in a bulk metallic glass under constrained and unconstrained condistions. Mater. Sci. Eng. A 771, 138585.

Cardinal, S., Pelletier, J.M., Xie, G.Q., Mercier, F., 2018. Manufacturing of cu-based metallic glasses matrix composites by spark plasma sintering. Mater. Sci. Eng. A 711, 405–414.

Du, Y., Han, W., Zhou, Q., Xu, Y., Zhai, H., Bhardwaj, V., Wang, H., 2020. Enhancing the plasticity of a Ti-based bulk metallic glass composite by cryogenic cycling treatments. J. Alloys Compd. 835, 155247.

Du, X., Huang, J.C., Hsieh, K-C., Jang, J.S.C., Liaw, P.K., Chen, H-M., Chou, H-S., Lai, Y-H., 2009. Designing ductile Zr-based bulk metallic glasses with phase separated microstructure. Adv. Eng. Mater. 11, 387–391.

Fan, J.J., Yan, Y.F., Chen, S.H., Ng, C-H., Wu, F.F., Chan, K.C., 2016. Reliability of the plastic deformation behavior of a Zr-based bulk metallic glass. Intermetallics 74, 25–30.

Fu, X., Wang, G., Wu, Y., Song, W., Shek, C.H., Zhang, Y., Shen, J., Ritchie, R.O., 2020. Compressive ductility and fracture resistance in CuZr-based shape-memory metallic-glass composites. Int. J. Plast. 128, 102687.

Gao, J., Sharp, J., Guan, D., Rainforth, W.M., Todd, I., 2015. New compositional design for creating tough metallic glass composites with excellent work hardening. Acta Mater. 86, 208–215.

Han, J., Jeong, U., Lee, Y., Marimuthu, K.P., Lee, H., 2021. Determination of parameters of free volume model for Zr-based BMG via nanoindentation. Intermetallics 131, 107121.

Henann, D.L., Anand, L., 2009. Fracture of metallic glasses at notches: Effects of notch-root radius and the ratio of the elastic shear modulus to the bulk modulus on toughness. Acta Mater. 57, 6057–6074.

Hofmann, D.C., 2013. Bulk metallic glasses and their composites: A brief history of diverging fields. J. Mater..

Holopainen, S., 2013. Modeling of the mechanical behavior of amorphous glassy polymers under variable loadings and comparison with state-of-the-art model predictions. Mech. Mater. 66, 35–58.

Holopainen, S., 2014. Influence of damage on inhomogeneous deformation behavior of amorphous glassy polymers, Modeling and algorithmic implementation in A finite element setting. Engng. Fract. Mech. 117, 28–50.

Holopainen, S., Barriere, T., 2018. Modeling of mechanical behavior of amorphous solids undergoing fatigue loadings, with application to polymers. Comput. Struct. 199, 57–73.

Holopainen, S., Wallin, M., 2012. Modeling of long-term behavior of amorphous glassy polymers. ASME J. Engng. Materials Technol. 135, 1–11.

Jiang, Y.P., Shi, X.P., Qiu, K., 2015. Numerical study of shear banding evolution in bulk metallic glass composites. Mater. Des. 77, 32–40.

Krämer, L., Champion, Y., Pippan, R., 2017. From powders to bulk metallic glass composites. Nat. Sci. Rep. 7, 6651–6659.

Kruzic, J.J., 2016. Bulk metallic glasses as structural materials: A review. Adv. Eng. Mater. 18, 1308–1331.

Lemaitre, J., Chaboche, J.L., 1999. Mechanics of Solid Materials. Cambridge University Press, Cambridge.

Lemaitre, J., Desmorat, R., 2001. Isotropic and anisotropic damage law of evolution. In: Lemaitre, J. (Ed.), Handbook of Materials Behavior Models. Academic Press, pp. 513–524.

Lin, W-H., Teng, Y., Sha, Z-D., Yuan, S-Y., 2020. Mechanical properties of nanoporous metallic glasses: Insights from large-scale atomic simulations. Int. J. Plast. 127, 102657.

Lu, Z., et al., 2021. Substantially enhanced plasticity of bulk metallic glasses by densifying local atomic packing. Nature Commun. 12, 6582.

Luo, J., Shi, Y., Picu, C.R., 2014. Shear-induced volumetric strain in CuZr metallic glass. Internat. J. Engrg. Sci. 83, 99–106.

Luo, L.S., Wang, B.B., Dong, F.Y., Su, Y.Q., Guo, E.Y., Xu, Y.J., Wang, M.Y., Wang, L., Yu, J.X., Ritchie, R.O., Guo, J.J., Fu, H.Z., 2019. Structural origins for the generation of strength, ductility and toughness in bulk-metallic glasses using hydrogen microalloying. Acta Materialia 171, 216–230.

Magagnosc, D.J., Kumar, G., Schroers, J., Felfer, P., Cairney, J.M., Gianola, D.S., 2014. Effect of ion irradiation on tensile ductility, strength and fictive temperature in metallic glass nanowires. Acta Materialia 74, 165–182.

Mu, X., Chellali, M.R., Boltynjuk, E., Gunderov, D., Valiev, R.Z., Hahn, H., Kübel, C., Ivanisenko, Y., Velasco, L., 2021. Unveiling the local atomic arrangements in the shear band regions of metallic glass. Adv. Mater. 33, 2007267.

Mukherjee, S., Schroers, J., Zhou, Z., Johnson, W.L., Rhim, W.K., 2004. Viscosity and spesific volume of bulk metallic glass-forming alloys and their correlation with glass forming ability. Acta Mater. 52, 3689–3695.

Pan, J., Ivanov, Y.P., Zhou, W.H., Li, Y., Greer, A.L., 2020. Strain-hardening and suppression of shear- banding in rejuvenated bulk metallic glass. Nature 578, 559–562.

Park, E.S., 2015. Understanding of the shear bands in amorphous metals. Appl. Microsc. 45, 63–73.

Pulidindi, K., Mukherjee, S., 2020. Metallic Glass Market Size 2020-2026. Report ID: GMI4722. Technical report, Global Market Insights.

Qiao, J.C., Pelletier, J.M., 2014. Dynamic mechanical relaxation in bulk metallic glasses: A review. J. Mater. Sci. Technol. 30, 523–545.

Qiao, J.C., Yao, Y., Pelletier, J.M., Keer, L.M., 2016. Understanding of micro-alloying on plasticity in $Cu_{46}Zr_{47-x}Al_7Dy_x$ $(0 \le x \le 8)$ bulk metallic glasses under compression: Based on mechanical relaxations and theoretical analysis. Int. J. Plast. 82, 62–75.

Qiu, F., Shen, P., Liu, T., Jiang, Q., 2012. Enhanced ductility in a $Zr_{65}Cu_{15}Al_{10}Ni_{10}$ bulk metallic glass by nanocrystallization during compression. Mater. Des. 36, 168–171.

Rao, W., Zhang, J., Kang, G.Z., Yu, C., Jiang, H., 2019. A meso-mechanical constitutive model of bulk metallic glass composites considering the local failure of matrix. Int. J. Plast. 115, 238–267.

Ravichandran, J.L.G., Johnson, W.L., 2003. Deformation behavior of the $Zr_{41.2}Ti_{13.8}Cu_{12.5}Ni_{10}$ $Be_{22.5}$ bulk metallic glass over a wide range of strain-rates and temperatures. Acta Mater. 51, 3429–3443.

Schuh, C.A., Hufnagel, T.C., Ramamurty, U., 2007. Mechanical behavior of amorphous alloys. Acta Mater. 144, 4067–4109.

Shahabi, H.S., Scudino, S., Kaban, I., Stoica, M., Rütt, U., Kühn, U., Eckert, J., 2015. Structural aspects of elasto-plastic deformation of a Zr-based bulk metallic glass under uniaxial compression. Acta Mater. 95, 30–36.

Singh, D., Mandal, R.K., Tiwari, R.S., Srivastava, O.N., 2016. Mechanical behavior of Zr-based metallic glasses and their nanocomposites. In: Movahedi, B. (Ed.), Metallic Glasses - Formation and Properties. IntechOpen.

Songa, J., Zhua, W., Wei, X., 2021. Correlations between the hierarchical spatial heterogeneity and the mechanical properties of metallic glasses. Int. J. Mech. Sci. 204, 106570.

Steif, P.S., Hutchinson, J.W., Spaepen, F., 1982. Strain localization in amorphous metals. Acta Metall. 30, 447–455.

Suryanarayana, C., 2012. Mechanical behavior of emerging materials. Mater. Today 15, 486–498.

Telford, M., 2004. The case for bulk metallic glass. Mater. Today 7, 36–43.

Tournier, R.F., 2016. Glass phase and other multiple liquid-to-liquid transitions resulting from two-liquid phase competition. Chem. Phys. Lett. 665, 64–70.

Wagner, H., Büchsenschütz-Göbeler, M., Luo, Y., Kumar, A., Arnold, W., Samwer, K., 2014. Measurement of local internal friction in metallic glasses. J. Appl. Phys. 115, 134307.

Wang, C., Cao, Q.P., Wang, X.D., Zhang, D.X., Ramamurty, U., Narayan, R.L., Jiang, J-Z., 2017. Intermediate temperature brittleness in metallic glasses. Adv. Mater. 29, 1605537.

Wang, T., Wu, Y., Si, J., Liu, Y., Hui, X., 2018. Plasticizing and work hardening in phase separated Cu-Zr-Al-Nb bulk metallic glasses by deformation induced nanocrystallization. Mater. Des. 142, 74–82.

Wei, R., Juan, Z., Guozheng, K., 2018. A failure mechanism based constitutive model for bulk metallic glass. Mech. Mater. 124, 52–69.

Wu, W.F., Li, Y., Schuh, C.A., 2008. Strength, plasticity and brittleness of bulk metallic glasses under compression: statistical and geometric effects. Phil. Mag. 1, 71–89.

Wu, Y., Xiao, Y., Chen, G., Liu, C.T., Lu, Z., 2010. Bulk metallic glass composites with transformation-mediated work-hardening and ductility. Adv. Mater. 22, 2770–2773.

Yanga, B., Liawa, P.K., Wanga, G., Morrisona, M., Liub, C.T., Buchanana, R.A., Yokoyama, Y., 2004. In-situ thermographic observation of mechanical damage in bulk-metallic glasses during fatigue and tensile experiments. Intermetallics 12, 1265–1274.

Yin, W., 2013. Compressive Behavior of Bulk Metallic Glass Under Different Conditions - Coupled Effect of Temperature and Strain Rate (Ph.D. thesis). The University of North Carolina, The United States.

Yuan, X., Sopu, D., Spieckermann, F., Song, K.K., Ketov, S.V., Prashanth, K.G., Eckert, J., 2022. Maximizing the degree of rejuvenation in metallic glasses. Scr. Mater 212, 114575.

Zhang, J., Jiang, H., Jiang, C., Kang, G., Lu, F., 2020. Stochastic deformation and shear transformation zones of the glassy matrix in CuZr-based metallic-glass composites. Int. J. Plast. 125, 52–62.

Zhao, J.X., Chen, Y.F., Wu, F.F., Gong, J.M., 2020. Numerical study on deformation behavior of bulk metallic glass composites via modified free-volume theory. Intermetallics 119, 106717.

Zhao, L., Han, D., Guan, S., Lu, X., Chan, K., Wang, G., 2021. Simultaneous improvement of plasticity and strength of metallic glasses by tailoring residual stress: Role of stress gradient on shear banding. Mater. Des. 197, 109246.

Zhao, J.X., Jiang, Y., Geng, L.Y., Gong, J.M., 2019. On the effect of hydrostatic stress on plastic deformation in metallic glasses. J. Non-Cryst. Solids 521, 119485.

Zhao, K., Xia, X.X., Bai, H.Y., Zhao, D.Q., Wang, W.H., 2011. Room temperature homogeneous flow in a bulk metallic glass with low glass transition temperature. Appl. Phys. Lett. 98, 141913.

Zhou, D., Hou, B., Li, B., Zhang, S., Dai, L., Li, Y., 2018. A comparative study of the rate effect on deformation mode in ductile and brittle bulk metallic glasses. Intermetallics 96, 94–103.

Zhou, J., Wang, Q., Zeng, Q., Yin, K., Wang, A., Luand, J., Sun, L., Shen, B., 2021. A plastic FeNi-based bulk metallic glass and its deformatin behavior. J. Mater. Sci. Technol. 76, 20–32.

Zhu, K., Tao, P., Zhang, C., Zhao, Z., Zhang, W., Yang, Y., Kaviyarasu, K., 2021. Effect of strain rates on the plastic deformation behavior and serrated flow of $Zr_{55.7}Cu_{22.4}Ni_{7.2}Al_{14.7}$ bulk metallic glass. Mater. Today Commun. 27, 102320.

Zhu, Z., Yi, C., Shi, T., Gao, Y., Wen, C., Liao, G., 2014. Fabricating Zr-based bulk metallic glass microcomponent by suction casting using silicon micromold. Adv. Mech. Eng. 2014, 1–8.

Zong, H., Bian, L., Cheng, J., Cao, G., Kang, C., Li, Ming, 2016. Glass forming ability, thermal stability and elastic properties of Zr-Ti-Cu-Be-(Fe) bulk metallic glasses. Results Phys. 6, 1157–1160.